NEAR FIELD MICROWAVE IMAGING TECHNIQUES FOR EMBEDDED OBJECT DETECTION AND SHAPE RECONSTRUCTION

A Thesis
presented to
the Faculty of the Graduate School
at the University of Missouri-Columbia

In Partial Fulfillment
of the Requirements for the Degree
Master of Science

---

by

SOMSAK TANTONG

Dr. Naz E. Islam   Thesis Supervisor

AUGUST 2007

The undersigned, appointed by the dean of the Graduate School, have examined the thesis entitled

NEAR FIELD MICROWAVE IMAGING TECHNIQUES FOR EMBEDDED

OBJECT DETECTION AND SHAPE RECONSTRUCTION

presented by Somsak Tantong,

a candidate for the degree of Master of Science in Electrical Engineering,

and hereby certify that, in their opinion, it is worthy of acceptance.

Naz E. Islam

Professor Naz E. Islam

William C. Nunnally

Professor William C. Nunnally

Jane M. Armer

Professor Jane M. Armer

ACKNOWLEDGEMENTS

NEAR FIELD MICROWAVE IMAGING TECHNIQUES FOR EMBEDDED OBJECT DETECTION AND SHAPE RECONSTRUCTION

Somsak Tantong

Dr. Naz E. Islam   Thesis Supervisor

ABSTRACT

A method for the detection, imaging and reconstruction of an embedded object through the application of a near field, frequency-synthesized microwave pulse is described. The work describes an alternate detection and reconstruction technique called the Single-Probe Imaging through Detection and Reconstruction (SPIDR) method, which uses a single near-field probe to locate the distance from an embedded object and then reconstruct the object's shape. The method described is both experiment and software driven, which carries out extensive data collection and processing computations. For complete image mapping and reconstruction, a combines scanning technique is employed since planar scanning alone cannot provide image reconstruction. The method described is applicable to symmetrical objects which can be extended to non-symmetrical objects through enhanced reconstruction methods.

NOMENCLATURE

Symbol	Definition	SI Units
λ	Wavelength	Meter
D	Longest dimension of aperture of the Antenna	Meter
S_{11}	Reflection measurement	(Dimensionless)
S_{12}	Transmission measurement	(Dimensionless)
S_{21}	Transmission measurement	(Dimensionless)
S_{22}	Reflection measurement	(Dimensionless)
V_n^+	Amplitude of the voltage wave incident at port n	Volt
V_n^-	Amplitude of the voltage wave reflected at port n	Volt
a	Waveguide height	Centimeter
b	Waveguide width	Centimeter
c	Pyramidal horn width	Centimeter
E_0^+	Initial amplitude of positive electric field	Volt/Meter (V/m)
E_0^-	Initial amplitude of negative electric field	Volt/Meter (V/m)
E^i	Incident electric field	Volt/Meter (V/m)
E^r	Reflected electric field	Volt/Meter (V/m)
E^t	Transmitted electric field	Volt/Meter (V/m)
E_x	Electric field of x component	Volt/Meter (V/m)
E_y	Electric field of y component	Volt/Meter (V/m)
E_z	Electric field of z component	Volt/Meter (V/m)
G_0	Desired Gain	(Dimensionless)
H_0^+	Initial amplitude of positive magnetic field	Ampere/Meter (A/m)
H_0^-	Initial amplitude of negative magnetic field	Ampere/Meter (A/m)
H^i	Incident magnetic field	Ampere/Meter (A/m)
H^r	Reflected magnetic field	Ampere/Meter (A/m)
H^t	Transmitted magnetic field	Ampere/Meter (A/m)
H_x	Magnetic field of x component	Ampere/Meter (A/m)
H_y	Magnetic field of y component	Ampere/Meter (A/m)
H_z	Magnetic field of z component	Ampere/Meter (A/m)
J_i	Impressed (source) electric current Density	Ampere/Meter^2 (A/m^2)
M_i	Impressed (source) magnetic current Density	Ampere/Meter^2 (A/m^2)
P_e	Electric field horn length	Centimeter
P_h	Magnetic field horn length	Centimeter

Z_w	Wave impedance	Ohm
β	Phase constant or wave number	Radian/Meter
β^i	Incident phase constant	Radian/Meter
β^r	Reflected phase constant	Radian/Meter
β^t	Transmitted phase constant	Radian/Meter
ε	Permittivity in a medium	Farads/Meter (F/m)
ε_r	Relative permittivity	Farads/Meter (F/m)
ε_1	Permittivity of medium 1	Farads/Meter (F/m)
ε_2	Permittivity of medium 2	Farads/Meter (F/m)
η	Intrinsic impedance in the free space (377 Ohm)	Ohm
η_1	Intrinsic impedance of medium 1	Ohm
η_2	Intrinsic impedance of medium 2	Ohm
σ	Conductivity in a medium	Siemens/Meter(S/m)
σ_1	Conductivity of medium 1	Siemens/Meter(S/m)
σ_2	Conductivity of medium 2	Siemens/Meter(S/m)
μ	Permeability in a medium	Henries/Meter (H/m)
μ_r	Relative permeability	Henries/Meter (H/m)
μ_1	Permeability of medium 1	Henries/Meter (H/m)
μ_2	Permeability of medium 2	Henries/Meter (H/m)
ω	Angular frequency	Radian/Second
T	Transmission coefficient	(Dimensionless)
Γ	Reflection coefficient	(Dimensionless)
T^b	Transmission coefficient at boundary	(Dimensionless)
Γ^b	Reflection coefficient at boundary	(Dimensionless)

LIST OF ACRONYMS

Acronyms	Definition
AUT	Antenna Under Test
ARC	Antenna Range Controller
CPS	Combined Planar Scan
CPU	Central Processing Unit
CS	Combined Scan
CST	Computer Simulation Technology
HP	Hewlet Packard products
HP-IB	Hewlet Packard Internal Bus
PS	Planar Scan
RF	Radio Frequency
RS	Rotational Scan
SPIDR	Single Probe Imaging through Detection and Reconstruction
VNA	Vector Network Analyzer

TABLE OF CONTENTS

LIST OF FIGURES

x

Chapter 1: Introduction

Electromagnetic fields in the microwave region play a significant role in many disciplines such as science, industry, military, medicine, etc. Microwave frequencies have been a subject of interest for several years and one of its many applications include devising mechanisms to detect embedded objects in a given medium, which is essentially accomplished through detection and image reconstruction. Some of the applications where microwave imaging can be of use are investigation of materials electromagnetic properties, nondestructive testing, determination of aircraft scattering characteristics, non- invasive medical diagnostics, aerial and aerial cover design, detection of objects buried in soil such as mines, cable and so on, There are various types of method and technique that have been utilized for the detection and reconstruction of embedded objects [1-5]. In this research we have introduced a new technique for detection and reconstruction.

Specifically, this work utilizes a near-field imaging technique using a single probe and is therefore called the Single Probe Imaging through Detection and Reconstruction (SPIDR). The objective of this method is to determine the location of a buried object in any given medium and the subsequent reconstruction of its image using a single probe. Theoretically, in electromagnetic detection method, the field region can be classified into two main regions: near-field and far-field zone and both regions can be employed to detect any given target. Using near field for detection and reconstruction, however, has its advantages. Since near-field ranges, specifically of microwave antennas, are very short the experimental setup and antennas required for measurements require very little space

as compared to the large distances required far-field image reconstruction. Moreover, near-field measurement can be interpreted to corresponding far-field pattern. The interpretation results are also used to determine the most common antenna characteristic such as radiation properties like directional pattern, gain or phase pattern etc in the far-field region [23].

The main interest of this study is to investigate electromagnetic signature of an object buried in a given medium in the near-field region, by using near-field scanning system, which consists of a pyramidal horn antenna, a network analyzer and by employing an image reconstruction technique to be described later in this work. This method is applicable to microwave frequencies ranging from 8.2 to 12.4 GHz for the detection, location and reconstruction of an embedded object.

A near-field scanner system is used to scan the electromagnetic field around the medium where the object buried. A vector Network Analyzer (VNA) is used to provide the transmitted and reflected signal measurement from the probe and the object, respectively. All of the recorded data from PC recorder are processed through an in-house developed code which will also be discussed in this research. Following this brief introduction, chapter 2 will start with the history and application of Breast Cancer Detection in various techniques. In Chapter 3 the several theories related with the measurement are described. Explanation over the experiment setup and its component, such as NSI system, Vector network analyzer, Scan modes, and measurement procedure are discussed in Chapter 4. The measurement results and discussion related with this experiment are detailed in Chapter 5. The last chapter, Chapter 6, point out the conclusion over the whole measurement and future work that can be done.

Chapter 2: Literature Review

An algorithm for early breast cancer detection in mammograms is described in a patent literature published in 1992. This study was suggested by Isaac N. Bankman, William A. Christens-Barry, Irvign N. Weinberg, Dong W. Kim, Ralph D. Semmel, and William R. Brody [6]. The algorithm is specifically designed for detecting clusters or micro calcifications that are early mammographic signs of breast cancer and can be implemented in a general purpose computer that will assist the radiologist by indicating the location of suspicious cluster. In 1994, a study of neural networks and higher order spectra for breast cancer detection was demonstrated by Tamia Stahaki, A.G. Constantinides [7]. In this paper, the results show significant discriminating gains through their technique applying higher order spectral estimation techniques for the derivation of the parameters of two dimensional autoregressive (AR) models.

In 1997, Infra-red imaging technique for Breast Cancer was proposed by Parvis Gamagami, Melmin J. Silverstein, James R. Waisman. The paper presents a reliable, and efficiency method of chemotherapy in inflammatory breast carcinoma. Infra-red heat detection was used in medicine in breast cancer. The result was very impressive [8].

In 2000, a study of microwave imaging technique for breast cancer detection has demonstrated by E.C.Fear and M.A. Stuchy [9]. In that paper, it shows a system for microwave breast cancer detection and the idea of microwave confocal imaging technique. This method was using a series of resistively loaded dipole antennas and the breast was immersed in a liquid with electrical properties similar to skin or breast tissue. It was also shown that all of the antennas exhibit broadband behavior and the tumor could

be detected by applying the skin subtracting method.

During this period, the study of image processing algorithm led to assist breast cancer detection in digital mammograms. The research utilizes images form the Digital Database for Screening Mammography (DDSM) and makes use of segmentation with fuzzy models and classification by the crisp k-nearest neighbor (k-nn) algorithm [10]. During the same time, the infrared imaging was developed by J.R. Keyserlingk, P.D.Ahlgren, E. Yu, N. Bleeiveau, M. Yassa [200]. Their goal was to show that high-resolution IR imaging provides additional safe, practical, and objective information when produced and interpreted by sufficiently trained breast physicians [11].

In 2001, a confocal microwave imaging algorithm for breast cancer detection was demonstrated by Xu Li and Susan C. Hagness [12]. In that paper, they presented a computationally efficient and robust image reconstruction algorithm by using an ultrawideband confocal microwave imaging system. In this method, each element of an antenna array sequentially transmits an ultra short pulse into the breast and collects the backscatter signal. The backscatter waveforms at all antennas are then time-shifts and added to create a synthetic focal point. Then, the scan performed and adjusted the distribution of time shift of the stored backscatter waveforms for each new focal point. In this year, there is a study of neural tool for breast cancer detection and classification in Magnetic Resonance Imaging (MRI). This paper is proposed by F.A. Cardillo, A. Starita, D. Caramella, A. Cilotti [13]. This study used a tool which was advanced neural architecture to exploit the major statistical relationships between the features of different tissue types.

During this year, 3-D finite element solver for MRI was developed by creating

suitably numerical models of anatomical geometries. This technique will provide the physician with quantitative data that can increase the probability of successful cancer detection and therapeutic treatment. This paper entitled Automatic Finite Element Mesh Generation from MRI Scans for Breast Cancer Investigations was proposed by Ziji Wu and John M. Sullivan, Jr. [14].

A study of microwave imaging for medical applications was demonstrated by Wael Saleh and Nasser Qaddoumi in 2003. This study was using non-invasive near-field microwave nondestructive testing techniques. The main idea is based on the ability of microwaves to penetrate deeply inside dielectric materials (breast tissues). It was shown that the lower the frequencies penetrate, the deeper in the breast tissue will be. However, the size of the waveguide sensor increase drastically at lower frequencies and consequently the resolution degrades rapidly. To overcome this problem, they were using open-ended rectangular waveguide sensors loaded with a dielectric material to inspect tumors inside the breast [15]. Recently, a paper by R.S. Yoon, T.P. Demonte, L. Organ, M.L.G. Joy entitled "Study of current density distribution in a non-invasive breast cancer detection device" [16], shows a new way for breast cancer detection by using a non-invasive breast cancer detection device. This study is based on the Homologous Electrical Difference Analysis (HEDA) method and requires a measurement of breast tissue impedance using 32 surface electrodes arranged in a circular fashion over the patient's breast. The procedure was applying small current and the tissue impedance values were then calculated from the voltage and current.

In the same period, the frequency responses of tumors were investigated by Xing Yun, Elise C. Fear and Ronald Johnston through the simple breast model using computer

simulation. Also the influence of a variety of parameters (e.g. tumor shape, size, location and depth) on the frequency response was examined [17].

In 2004, the modeling of breast tissue with Finite difference time domain (FDTD) for microwave breast cancer detection is suggested by Panagiotis Kosmas, Carey M. Rappaport, and Emmett Bishop [18]. They introduced the effect of certain parameters of the detection problem and the 3-D FDTD modeling of the frequency dependence for the various types of tissue based on data frequency range of 30 MHz-20 GHz. In the same period, another technique for a simplified model of mammography geometry with electrical impedance tomography was proposed by Myong H. Dhoi, Tzu-Jen Kao, David Isaacson, Gary J. Saulnier, and Jonathan C. Newell. This method investigates a simplified model of the mammography geometry which is modeled as a rectangular box with electrode arrays on the top and the bottom planes. It was also shown the effect of electrode thickness and the resulting electrode side surface [19].

The tissue sensing adaptive radar (TSAR) for breast cancer detection - experimental investigation of simple tumor models was demonstrated by Jeff M. Sill and Elise C. Fear in 2005 [20], An analytical technique based on the differences in electrical properties between healthy and malignant tissues. They test and characterize the antenna, implement an improved TSAR algorithm, and detect tumors in a realistic breast model. In the same period, the application of multi-look in UWB microwave imaging for early breast cancer detection using hemispherical breast model was introduced by Beibei Zhou, Wenyi Shao, and Gang Wang. In that paper, the FDTD simulation and imaging reconstruction were used and the simulation results show that multi-look excels single-look method in multi-target detection and it can also reduce clutters in imaging results.

The study of ultra wideband microwave imaging via space–time beamforming for early-stage breast-cancer detection was carried out by Xu Li, Essex J. Bond, Barry D, Ban Veen, and Susan C. Hagness in 2005 [21]. The paper describes the concept of microwave imaging via space-time (MIST) beamforming and related signal-processing algorithms. The signal-processing technique is used to form a spatial image of scattered microwave energy, and to identify the presence and location of malignant lesions from their scattering signatures. The experimental feasibility of UWB microwave imaging was demonstrated to identify the presence and location of the targets by their scattering signature.

As recently as 2006, the experimental and theoretical investigation into a microwave breast cancer detection system was proposed by Wee Chang Khor, Hua Wang, Marek E. Bialkowski and Stuart Crozier. The special calibration technique for the Vector Network Analyser was employed to enhance breast cancer detection or target [5]. Also in this year, the study of near-field imaging for breast cancer detection by ultra wideband minimum variance beamforming was suggested by Wanjun Zhi, Francois Chin, and Michael Yan-Wah Chia. In that paper, the method, coherent-signal-subspace-based wideband minimum variance beamforming, was applied to the computed FDTD data to implement the simulation. The results show that the tumor is clearly identified and localized [22].

Chapter 3: Theoretical Background

3.1 Near-field System Conception

In this study, measurements in near-field region were considered. In this region the averaging energy density remains fairly constant at different distances from the antenna. Theoretically, the antenna field zones (shown in Figure 3.1.1) are divided into two principal regions; i) the near-field or Fresnel zone near the antenna and, ii) the far-field or Fraunhofer zone at a large distance. Near-field can be further categorized into two regions of interest, defined as the reactive near-field which is of immediate vicinity to the antenna and the radiating near-field region which lies next to the reactive near field region [23]. In the near-field or Fresnel region, the shape of the field pattern depends, in general, on the distance. The longitudinal component of the electric field is significant and power flow is not entirely radial.
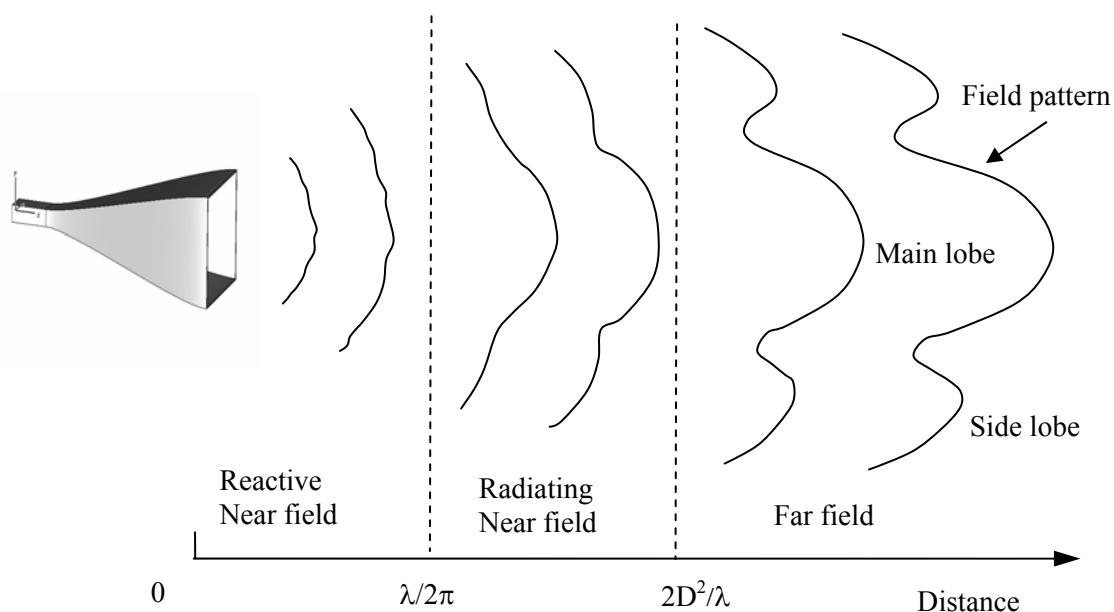

Figure 3.1.1 Regions of interest of surrounding antenna

The reactive or evanescent near-field region is the closet region in the vicinity of the antenna. In this region, the component of electromagnetic energy reduces rapidly with the distance from the antenna. Its range is usually within one wavelength of the antenna. It is seldom used for any measurement, because it normally is located too close to the antenna and mutual impedance caused by reactive coupling between the antennas makes the antenna measurement complicated. The range of this region starts at the antenna to the distance R_{reactive} which is set as

$$R_{reactive} = \frac{\lambda}{2\pi}$$ (3.1.1)

The Fraunhofer region, also known as far-field region, is the farthest region from the antenna. The range of this region starts at distance $R_{\text{far-field}}$ which is set as

$$R_{far-field} = \frac{2D^2}{\lambda}$$ (3.1.2)

where D is the largest dimension of the physical aperture of the antenna and λ is the wavelength. The main disadvantage of the far-field measurement is the required large distance to make any measurement. The distance can be too large for the measurement or it can result in atmospheric attenuation.

There are several advantages of the near-field measurement: electromagnetic field energy densities remain relatively constant, a little space is required to perform the measurement. Moreover, the results can be interpreted to equivalent far-field by using mathematical transform which is applied Fast Fourier Transform technique. There are two basic procedures to determine the equivalent far-field pattern. First, the phase front measurement procedure using a microwave interferometer probe positioned by scanner of

NSI system. A phase front is defined as a surface of equal phase. Near-field system consists of three elements: a robotic scanner including an optics system for precise measurement of probe position, an RF Subsystem, and a computer subsystem The RF subsystem consists of a microwave receiver connected to a field probing antenna. The probe antenna is moved under computer control over a planar, cylindrical, or spherical surface around the Antenna Under Test (AUT). The near-field range determines the equivalent far-field antenna performance through two basic steps [24]:

1. It measures the AUT's phase and amplitude at known positions.

2. It applies a Fourier transform to the measured data to evaluate its performance in the far-field.

The NSI program has two main program sections; data acquisition and data processing. In addition, there are several other sections which help analyze and process the data. Figure 3.1.2 shows a block diagram for a near-field measurement system configured with the AUT.
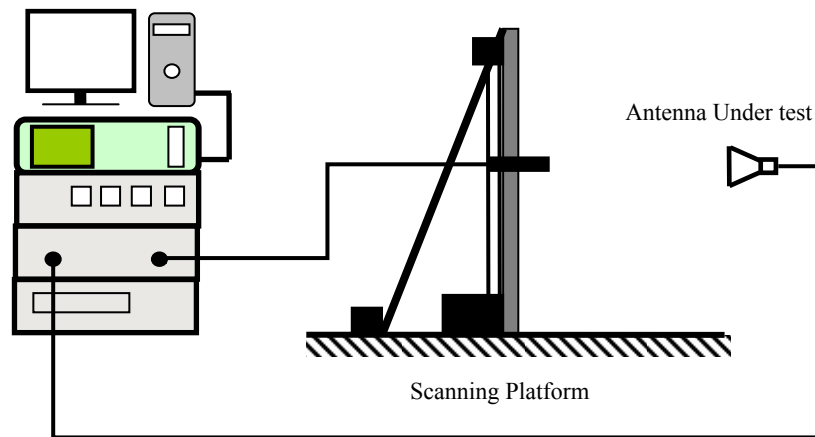
Figure 3.1.2 Near Field Measurement System Block Diagram

Near-field scanner system, provided by NSI Inc. has been extensively used to measure electromagnetic signature for detection, location and reconstruction of an embedded object. Near-field system is primarily used to determine parameters of an antenna such as the antenna gain, pattern, polarization and directivity. It provides a fast and accurate method for determining the performance of medium to high gain antennas, beamwidth, beam pointing phase center position, defocusing, autotrack (monopulse) bias, scale factor, linearity, phased array element excitation and reflector surface distortion measurements. Besides the parameters of the near-field, it also has the capability for computer controlled multi-frequency, multi-beam antenna measurements, far-field pattern computation based on near-field parameter. Hence, the near-field measurement can be completed in closed room. Antenna measurements by this method can provide significant advantages over competing techniques such as very high accuracy, high throughput, complete characterization of the antenna performance, control of zero G effects, minimal real estate requirements, elimination of delay due to weather;

measurements can be made in the antenna assembly area, compatible with special project security requirements.

Theoretically, an antenna is a transducer to transform a high frequency electric current to radio waves and vice versa. An antenna is used to transmit and receive radio waves. There are many kinds of antenna ranging from very small size antenna such as a monopoly antenna to very large antenna of 100 meters in diameter for radio wave astronomy. In this experiment, we are focusing on aperture antennas used for microwave remote sensing. Aperture antenna is a device that converts between guided electromagnetic wave in coaxial cable and those that propagating in the free space. The electromagnetic field properties change gradually with distance from the antenna. A horn antenna is regarded as a flared-out (or open-out) waveguide. The function of the horn is to produce a uniform phase front with a larger aperture than that of the waveguide and hence greater directivity. To minimize reflections of the guided wave, the transition region or horn between the waveguide at the throat and free space at the aperture could be given at gradual exponential taper.

3.2 The Scattering Matrix

In order to determine the location and reconstruction a buried object in any given medium, the transmitted and reflected signal measurement expressed in scattering-matrix form needs to be utilized. The theory behind the scattering matrix can be explained as follow. The scattering matrix provides a complete description of the network as seen as its N ports and relates the incident wave on the ports to those reflected from the ports. The scattering matrix representation is especially useful at high frequencies where it is difficult to measure total voltages and currents, but easier to measure incident and reflected voltages [25]. For this experiment, the scattering parameters can be measured directly with a vector network analyzer (VNA) which is HP8510b OPT 010. The scattering matrix, or S-parameter, is defined in relation to the incident and reflected voltage wave as

$$
\begin{bmatrix} V_1^- \\ V_2^- \\ \cdot \\ \cdot \\ \cdot \\ V_N^- \end{bmatrix} = \begin{bmatrix} S_{11} & S_{12} & \cdot & \cdot & \cdot & S_{1N} \\ S_{21} & \cdot & \cdot & \cdot & \cdot & \cdot \\ \cdot & \cdot & \cdot & \cdot & \cdot & \cdot \\ \cdot & \cdot & \cdot & \cdot & \cdot & \cdot \\ \cdot & \cdot & \cdot & \cdot & \cdot & \cdot \\ S_{N1} & \cdot & \cdot & \cdot & \cdot & S_{NN} \end{bmatrix} \begin{bmatrix} V_1^+ \\ V_2^+ \\ \cdot \\ \cdot \\ \cdot \\ V_N^+ \end{bmatrix}
\tag{3.2.1}
$$

$$
[V^-] = [S][V^+]
\tag{3.2.2}
$$

A particular element of the $[S]$ matrix can be found as

$$
S_{ij} = \left. \frac{V_i^-}{V_j^+} \right|_{V_k^+ = 0 \, for \, k \neq j}
\tag{3.2.3}
$$

where for n port network, V_n^+ is the amplitude of the voltage wave incident at port n, and V_n^- is the amplitude of the voltage wave reflected from port n.

3.3 Pyramidal Horn Antenna Characteristic

The pyramidal horn antenna used in the experiment is Narda model 640 pyramidal horn types. This probe is shown in Figure 3.3.1. It has radiation pattern having minimum side lobes and is fed by coaxial line using coax-to-waveguide adapter. The probe is able to operate in *X*-band frequency range of 8.2 to 12.4 GHz. The maximum VSWR is 1.15. Beam width in *E* and *H* plane varies from 23° at the highest frequency to 34° at the lowest frequency. Side lobes in the *H* plane are 13 dB down, second side lobes are 18 dB down and all other *E* plane lobes are more than 20 dB down. Gain at middle frequency is 22.5 dB. The probe dimension and gain characteristics are shown in Figure 3.3.2

Figure 3.3.1 Narda model 640 pyramidal horn antenna
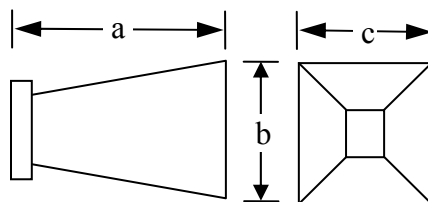
a = 12.86 cm, b = 7.86 cm, c = 5.95 cm

Figure 3.3.2 Pyramidal horn dimension

3.4 Plane Wave Propagation

The main focus of this research is to extract useful information from wave propagation to and reflected from the buried object. However, it is important to understand the plane wave propagation with normal and oblique incidence. In order to gain better understanding, this section will be discussed the wave propagation of plane wave at both normal and oblique incidence.

3.4.1 Normal Incidence

We begin the discussion of reflection and transmission from planar boundaries of lossless media and source-free by assuming that the wave travel is perpendicular to the planar interface [26]. The wave propagating is incident normally on the boundary $z = 0$ from medium 1 characterized by μ_1, ε_1, σ_1 medium 2 characterized by μ_2, ε_2, σ_2 as shown in Figure 3.4.1
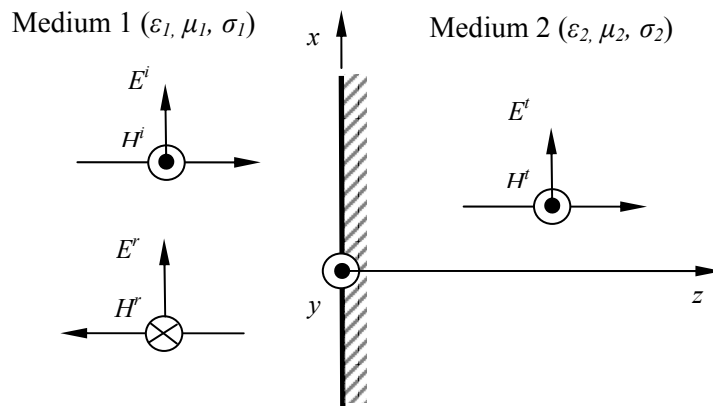

Figure 3.4.1 Wave reflection and transmission at normal incidence

For source-free and lossless media, the electric field has only an x component, it must satisfy the wave equation of

$$\nabla^2 E_x(x,y,z) + \beta^2 E_x(x,y,z) = 0, \tag{3.4.1}$$

$$\frac{\partial^2 E_x}{\partial x^2} + \frac{\partial^2 E_x}{\partial y^2} + \frac{\partial^2 E_x}{\partial z^2} + \beta^2 E_x = 0. \tag{3.4.2}$$

Whose solution is given by

$$E_x(x,y,z) = f(x)g(y)h(z). \tag{3.4.3}$$

Because the uniform plane wave travels in z direction, its solution is not a function of x and y. Therefore Eq.3.4.3 reduces to

$$E_x(z) = h(z)$$

$$E_x(z) = E_0^+ e^{-j\beta z} + E_0^- e^{+j\beta z} = E_x^+ + E_x^- \tag{3.4.4}$$

$$E_x^+ = E_0^+ e^{-j\beta z} \tag{3.4.5}$$

$$E_x^- = E_0^- e^{+j\beta z} \tag{3.4.6}$$

where E_0^+ and E_0^- represent, respectively, the amplitudes of the positive and negative in z direction of traveling wave. In this experiment, there are 2 media which are characterized by the constitutive parameters of ε_1, μ_1, and ε_2, μ_2. The reflection and transmission from planar boundaries of lossless media in z direction is perpendicular (normal incident) to the planar interface lossless media, where the incident wave encounters the interface, a fraction of the wave intensity will be reflected into medium 1 and part will be transmitted into medium 2. In this case, the incident electric field of amplitude E_0 is polarized in the x direction (see Figure.3.4.1), we can write the expressions for its incident, reflected, and transmitted electric field components, respectively, as

$$E^i = \hat{a}_x E_0 e^{-j\beta_1 z} \quad \text{(Incident in positive } z\text{-direction)} \tag{3.4.7}$$

$$E^r = \hat{a}_x \Gamma^b E_0 e^{+j\beta_1 z} \quad \text{(Reflected in negative } z\text{-direction)} \tag{3.4.8}$$

$$E^t = \hat{a}_x T^b E_0 e^{-j\beta_2 z} \quad \text{(Transmitted in positive } z\text{-direction)} \tag{3.4.9}$$

where Γ^b and T^b represent, respectively, the reflection and transmission coefficients at the interface. Since the incident fields are linearly polarized and the reflecting surface is planar, the reflected and transmitted fields will be linearly polarized.

Since the electric field is known, as given by Eq.3.4.4, the magnetic field can be determined by using Maxwell's equation

$$\nabla \times E = -j\omega\mu H , \tag{3.4.10}$$

$$H_y = -\frac{1}{j\omega\mu} \nabla \times E_x , \tag{3.4.11}$$

where
$$\nabla \times E_x = \begin{vmatrix} \hat{a}_x & \hat{a}_y & \hat{a}_z \\ \dfrac{\partial}{\partial x} & \dfrac{\partial}{\partial y} & \dfrac{\partial}{\partial z} \\ E_x & 0 & 0 \end{vmatrix} ,$$

$$H_y = -\frac{1}{j\omega\mu} \left\{ \hat{a}_x (0) + \hat{a}_y \left(\frac{\partial E_x}{\partial z} \right) - \hat{a}_z \left(\frac{\partial E_x}{\partial y} \right) \right\} , \tag{3.4.12}$$

$$H_y = -\hat{a}_y \frac{1}{j\omega\mu} \left\{ \frac{\partial E_x}{\partial z} \right\} . \tag{3.4.13}$$

Substituting E_x Eq.3.4.4 into Eq.3.4.13;

$$H_y = -\hat{a}_y \frac{1}{j\omega\mu} \left\{ \frac{\partial (E_0^+ e^{-j\beta Z} + E_0^- e^{+j\beta Z})}{\partial z} \right\} , \tag{3.4.14}$$

$$H_y = \hat{a}_y \frac{\beta}{\omega\mu} \left\{ E_0^+ e^{-j\beta Z} - E_0^- e^{+j\beta Z} \right\} . \tag{3.4.15}$$

From $\beta^2 = \omega^2 \mu\varepsilon$,

$$H_y = \hat{a}_y \frac{1}{\sqrt{\mu/\varepsilon}} \left\{ E_0^+ e^{-j\beta Z} - E_0^- e^{+j\beta Z} \right\}, \qquad (3.4.16)$$

$$H_y = \hat{a}_y \frac{1}{\sqrt{\mu/\varepsilon}} \left\{ E_x^+ - E_x^- \right\}, \qquad (3.4.17)$$

$$H_y = \hat{a}_y \left\{ H_y^+ + H_y^- \right\}, \qquad (3.4.18)$$

where $H_y^+ = \hat{a}_y \dfrac{1}{\sqrt{\mu/\varepsilon}} E_x^+, \qquad H_y^- = -\hat{a}_y \dfrac{1}{\sqrt{\mu/\varepsilon}} E_x^-$

Wave impedance (Zw) is the ratio of the electric to magnetic field represented by

$$Z_w = \frac{E_x^+}{H_y^+} = -\frac{E_x^-}{H_y^-} = \eta = \sqrt{\frac{\mu}{\varepsilon}} . \qquad (3.4.19)$$

The magnetic field components corresponding to electric field Eq.3.4.7 through Eq.3.4.9 can be written as

$$H^i = \hat{a}_y \frac{E_0}{\eta_1} e^{-j\beta_1 Z} \qquad \text{(Incident in positive z-direction)} \qquad (3.4.20)$$

$$H^r = -\hat{a}_y \frac{\Gamma^b E_0}{\eta_1} e^{+j\beta_1 Z} \quad \text{(Reflection in negative z-direction)} \qquad (3.4.21)$$

$$H^t = \hat{a}_y \frac{T^b E_0}{\eta_2} e^{-j\beta_2 z} \quad \text{(Transmission in positive z-direction)} (3.4.22)$$

The reflection and transmission coefficients will now be determined by enforcing continuity of the tangential components of the electric and magnetic fields across the interface. Using Eq.3.4.7 through Eq.3.4.9 and Eq.3.4.20 through Eq.3.4.22, continuity of the tangential components of the electric and magnetic fields at the interface (z =0) leads, respectively, to

$$1 + \Gamma^b = T^b \qquad (3.4.23)$$

$$\frac{1}{\eta_1}(1 - \Gamma^b) = \frac{1}{\eta_2} T^b \tag{3.4.24}$$

Solving 2 equations for Γ^b and T^b, we can write that

$$\Gamma^b = \frac{\eta_2 - \eta_1}{\eta_1 + \eta_2} = \frac{E^r}{E^i} = -\frac{H^r}{H^i} \tag{3.4.25}$$

$$T^b = \frac{2\eta_2}{\eta_1 + \eta_2} = 1 + \Gamma^b = \frac{E^t}{E^i} = -\frac{\eta_2}{\eta_1} \frac{H^t}{H^i} \tag{3.4.26}$$

3.4.2 Oblique Incidence

In order to analyze the reflections and transmissions at oblique wave incidence, we need to introduce the plane of incidence, which is defined as the plane formed by a unit vector normal to the reflecting interface and the vector in the direction of incidence. For a wave whose wave vector is on the *xz* plane and is incident upon an interface that is parallel to the *xy* plane as shown in Figure 3.4.2, the plane of incidence is the *xz* plane [26].

To determine the reflections and transmissions at oblique angles of incidence for a general wave polarization, it is most convenient to decompose the electric field into its perpendicular and parallel components (relative to the plane of incidence) and analyze each one of them individually. The total reflected and transmitted field will be the vector sum from each one of these two polarizations.

When the electric field is perpendicular to the plane of incidence, the polarization of the wave is referred to as perpendicular polarization. Since the electric field is parallel to the interface, it is also known as horizontal or *E* polarization. When the electric field is parallel to the plane of incidence, the polarization is referred to as parallel polarization. Because a component of the electric field is also perpendicular to the interface when the

19

magnetic field is parallel to the interface, it is also known as vertical or *H* polarization. Each type of polarization will be further examined.

1. Perpendicular (Horizontal or *E*) Polarization: assuming the electric field of the uniform plane wave incident on a planar interface at an oblique angle, as shown in Figure 3.4.2, is oriented perpendicularly to the plane of incidence.
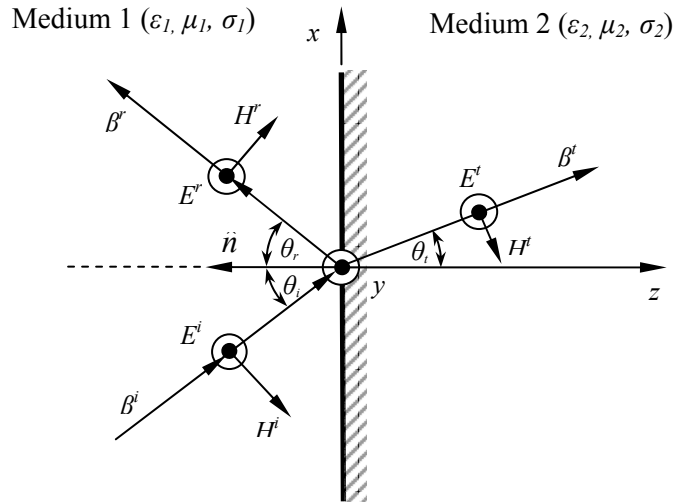

Figure 3.4.2 Perpendicular (horizontal) polarized uniform plane wave incident at an oblique angle on an interface

The incident electric and magnetic fields can be written as

$$E^i = \hat{a}_y E^i e^{-j\beta^i \cdot r} = \hat{a}_y E_0 e^{-j\beta_1 (x \sin\theta_i + z \cos\theta_i)} \tag{3.4.27}$$

$$H^i = (-\hat{a}_x \cos\theta_i + \hat{a}_z \sin\theta_i) H^i e^{-j\beta^i \cdot r}$$

$$= (-\hat{a}_x \cos\theta_i + \hat{a}_z \sin\theta_i) \frac{E_0}{\eta_1} e^{-j\beta_1 (x \sin\theta_i + z \cos\theta_i)} \tag{3.4.28}$$

where

$$E^i = E_0 \tag{3.4.29}$$

$$H^i = \frac{E^i}{\eta_1} = \frac{E_0}{\eta_1} \tag{3.4.30}$$

20

Similarly the reflected field can be expressed as

$$E^r = \hat{a}_y E^r e^{-j\beta^r \cdot r} = \hat{a}_y \Gamma^b E_0 e^{-j\beta_1(x\sin\theta_r + z\cos\theta_r)} \tag{3.4.31}$$

$$H^r = (\hat{a}_x \cos\theta_r + \hat{a}_z \sin\theta_r) H^r e^{-j\beta^i \cdot r}$$

$$= (\hat{a}_x \cos\theta_r + \hat{a}_z \sin\theta_r) \frac{\Gamma^b E_0}{\eta_1} e^{-j\beta_1(x\sin\theta_r + z\cos\theta_r)} \tag{3.4.32}$$

where

$$E^r = \Gamma^b E^i = \Gamma^b E_0 \tag{3.4.33}$$

$$H^r = \frac{E^r}{\eta_1} = \frac{\Gamma^b E_0}{\eta_1} \tag{3.4.34}$$

Also the transmitted fields can be written as

$$E^t = \hat{a}_y E^t e^{-j\beta^t \cdot r} = \hat{a}_y T^b E_0 e^{-j\beta_2(x\sin\theta_t + z\cos\theta_t)} \tag{3.4.35}$$

$$H^t = (-\hat{a}_x \cos\theta_t + \hat{a}_z \sin\theta_t) H^t e^{-j\beta^t \cdot r}$$

$$= (-\hat{a}_x \cos\theta_t + \hat{a}_z \sin\theta_t) \frac{T^b E_0}{\eta_2} e^{-j\beta_2(x\sin\theta_t + z\cos\theta_t)} \tag{3.4.36}$$

where

$$E^t = T^b E^t = T^b E_0 \tag{3.4.37}$$

$$H^t = \frac{E^t}{\eta_2} = \frac{T^b E_0}{\eta_2} \tag{3.4.38}$$

The reflection Γ^b and transmission T^b coefficients, and the relation between the incident θ_i, reflected θ_r, and transmission (refracted) θ_t angles can be obtained by applying the boundary conditions on the continuity of the tangential components of the electric and magnetic fields. The reflection coefficient can be written as

$$\Gamma^b = \frac{E^r}{E^i} = \frac{\eta_2 \cos\theta_i - \eta_1 \cos\theta_t}{\eta_2 \cos\theta_i + \eta_1 \cos\theta_t} = \frac{\sqrt{\dfrac{\mu_2}{\varepsilon_2}}\cos\theta_i - \sqrt{\dfrac{\mu_1}{\varepsilon_1}}\cos\theta_t}{\sqrt{\dfrac{\mu_2}{\varepsilon_2}}\cos\theta_i + \sqrt{\dfrac{\mu_1}{\varepsilon_1}}\cos\theta_t} \qquad (3.4.39)$$

The reflection coefficient can be written as

$$T^b = \frac{E^t}{E^i} = \frac{2\eta_2 \cos\theta_i}{\eta_2 \cos\theta_i + \eta_1 \cos\theta_t} = \frac{2\sqrt{\dfrac{\mu_2}{\varepsilon_2}}\cos\theta_i}{\sqrt{\dfrac{\mu_2}{\varepsilon_2}}\cos\theta_i + \sqrt{\dfrac{\mu_1}{\varepsilon_1}}\cos\theta_t} \qquad (3.4.40)$$

Γ^b and T^b are usually referred to as the plane wave *Fresnel reflection and transmission coefficients* for perpendicular polarization.

2. Parallel (Vertical or *H*) Polarization: for this polarization, the electric field is parallel to the plane of incidence and it impinges upon a planar interface as shown in Figure 3.4.3. The directions of the incident, reflected, and transmitted electric and magnetic fields are shown in Figure 3.4.3.
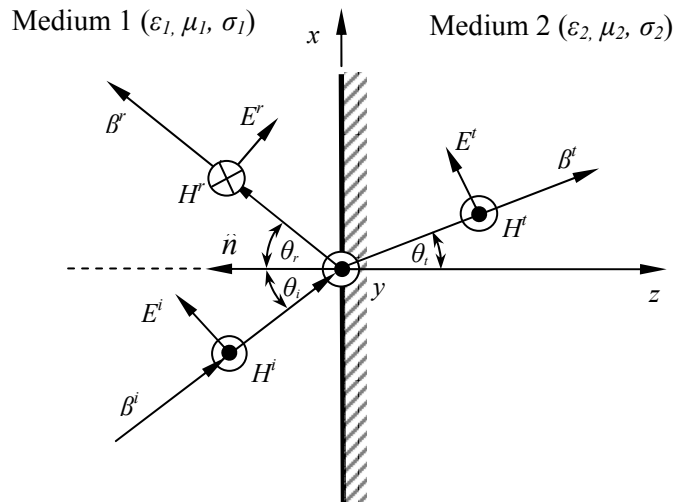

Figure 3.4.3 Parallel (vertical) polarized uniform plane wave incident at an oblique angle on an interface

The incident electric and magnetic fields can be written as

$$E^i = (\hat{a}_x \cos\theta_i - \hat{a}_z \sin\theta_i)E_0 e^{-j\beta^i \cdot r}$$

$$= (\hat{a}_x \cos\theta_i - \hat{a}_z \sin\theta_i)E_0 e^{-j\beta_1(x\sin\theta_i + z\cos\theta_i)} \qquad (3.4.41)$$

$$H^i = \hat{a}_y H^i e^{-j\beta^i \cdot r} = \hat{a}_y \frac{E_0}{\eta_1} e^{-j\beta_1(x\sin\theta_i + z\cos\theta_i)} \qquad (3.4.42)$$

where

$$E^i = E_0 \qquad (3.4.43)$$

$$H^i = \frac{E^i}{\eta_1} = \frac{E_0}{\eta_1} \qquad (3.4.44)$$

Similarly the reflected field can be expressed as

$$E^r = (\hat{a}_x \cos\theta_r + \hat{a}_z \sin\theta_r)E^r e^{-j\beta^r \cdot r}$$

$$= (\hat{a}_x \cos\theta_r + \hat{a}_z \sin\theta_r)\Gamma^b E_0 e^{-j\beta_1(x\sin\theta_r + z\cos\theta_r)} \qquad (3.4.45)$$

$$H^r = -\hat{a}_y H^r e^{-j\beta^r \cdot r} = -\hat{a}_y \frac{\Gamma^b E_0}{\eta_1} e^{-j\beta_1(x\sin\theta_r + z\cos\theta_r)} \qquad (3.4.46)$$

where

$$E^r = \Gamma^b E^i = \Gamma^b E_0 \qquad (3.4.47)$$

$$H^r = \frac{E^r}{\eta_1} = \frac{\Gamma^b E_0}{\eta_1} \qquad (3.4.48)$$

Also the transmitted fields can be written as

$$E^t = (\hat{a}_x \cos\theta_t - \hat{a}_z \sin\theta_t)E^t e^{-j\beta^t \cdot r}$$

$$= (\hat{a}_x \cos\theta_t - \hat{a}_z \sin\theta_t)T^b E_0 e^{-j\beta_2(x\sin\theta_t + z\cos\theta_t)} \qquad (3.4.49)$$

$$H^t = \hat{a}_y H^t e^{-j\beta^t \bullet r} = \hat{a}_y \frac{T^b E_0}{\eta_2} e^{-j\beta_2(x\sin\theta_t + z\cos\theta_t)} \qquad (3.4.50)$$

where

$$E^t = T^b E^i = T^b E_0 \qquad (3.4.51)$$

$$H^t = \frac{E^t}{\eta_2} = \frac{T^b E_0}{\eta_2} \qquad (3.4.52)$$

The reflection Γ^b and transmission T^b coefficients, and the relation between the incident θ_i, reflected θ_r, and transmission (refracted) θ_t angles can be obtained by applying the boundary conditions on the continuity of the tangential components of the electric and magnetic fields. The reflection coefficient can be written as

$$\Gamma^b = \frac{\eta_2 \cos\theta_t - \eta_1 \cos\theta_i}{\eta_2 \cos\theta_t + \eta_1 \cos\theta_i} = \frac{\sqrt{\dfrac{\mu_2}{\varepsilon_2}}\cos\theta_t - \sqrt{\dfrac{\mu_1}{\varepsilon_1}}\cos\theta_i}{\sqrt{\dfrac{\mu_2}{\varepsilon_2}}\cos\theta_t + \sqrt{\dfrac{\mu_1}{\varepsilon_1}}\cos\theta_i} \qquad (3.4.53)$$

The reflection coefficient can be written as

$$T^b = \frac{2\eta_2 \cos\theta_i}{\eta_2 \cos\theta_t + \eta_1 \cos\theta_i} = \frac{2\sqrt{\dfrac{\mu_2}{\varepsilon_2}}\cos\theta_i}{\sqrt{\dfrac{\mu_2}{\varepsilon_2}}\cos\theta_t + \sqrt{\dfrac{\mu_1}{\varepsilon_1}}\cos\theta_i} \qquad (3.4.54)$$

Γ^b and T^b are usually referred to as the plane wave *Fresnel reflection and transmission coefficients* for parallel polarization.

Chapter 4: Experimental and Simulation Configuration

4.1 Near-field System

The NSI system was used to conduct the near-field scanning experiment. This system consists of a mechanical scanning platform in the *X-Y* direction with resolution of 0.1mm [28]. The scanning platform supports a Narda model 640 pyramidal horn antenna which operates in the *X*-band frequency range from 8.2 to 12.4 GHz. The probe is connected to coaxial waveguide adapter (X281C) and then to 85131F NMD-3.5 mm. Flexible Test Port Cables. The cable length is 62.2 cm. (24.5 inches) connected to the *S*-parameter test set. The scanning platform is controlled by a computer controller and servo motors. The pyramidal horn is horizontally placed at the origin so that the electric field vector is oriented in the *y*-direction (magnetic field vector in the *x*-direction). Consequently, the incident wave is perpendicularly polarized. The NSI scanner is illustrated in Figure 4.1.1.
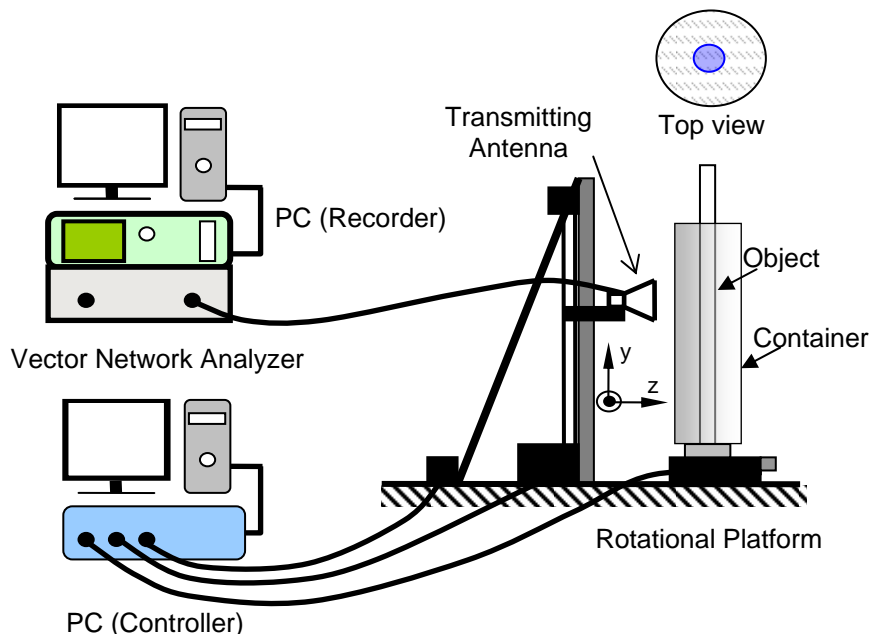

Fig. 4.1.1 Configuration of the Near-field system

This system is capable of planar, rotational and cylindrical scan. The *x*-axis movement is represented by the movement of the probe to left and right direction while the *y*-axis movement is represented by the movement of the probe to up and down direction. The rotational movement of the object is represented by rotating the rotational platform over the azimuth axis. For planar, rotational and cylindrical scan mode, the probe will take measurement over *x*-axis, azimuth-axis, and x-azimuth axis, respectively. The topic of the three scanning modes will be discussed more extensively in section 4.3 since all measurements, probe and object detection and reconstruction were taken using these types of scanning. The embed object and antenna configuration is shown in Figure 4.1.2. The plastic container can be filled with air water or oil. The plastic container diameter is 15.00 cm. Cylindrical-aluminum object has a diameter of 1.25 cm.
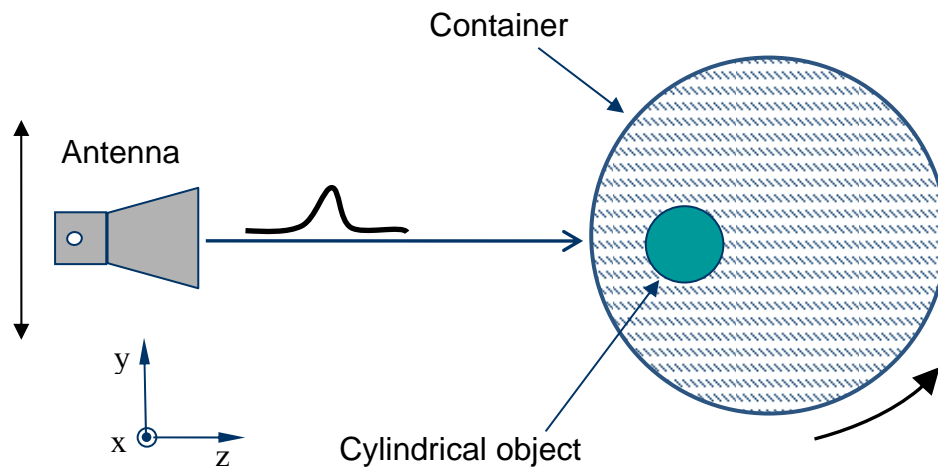

Fig. 4.1.2 Antenna and object Configuration

4.2 Vector Network Analyzer

The *vector network analyzer* (VNA) used in the experimental setup is HP8510B OPT010 and consists of three components: source generator, *S*-parameter test set, and phase coherent receiver. The VNA, which capability of broadband measurement from 45 MHz to 40 GHz in coax, and up to 110 GHz in waveguide bands is used to measure complex (magnitude and phase) reflection and transmission and group delay of two-port networks (*S*-parameter) to characterize their linear behavior. It has a functional capability of displaying a network's time domain and response to an impulse or a step waveform by computing the inverse Fourier transform of the frequency domain response. The transform technique using in this Analyzer is Inverse Chirp-Z transform (ICZT).

The synthesized sweeper microwave source in this experiment is HP83622A. Its operated range frequency for this source is from 2 GHz to 20 GHz. The RF energy from the source will be provided directly to the *S*-parameter test set which is HP8515A. This *S*-parameter test set consists of 2 port connections (port 1, port 2) and has maximum input power of HP8515A at +14 dBm with connector type 3.5 mm female. It also has two separate transmission (S_{12}, S_{21}) and reflection (S_{11}, S_{22}) measurements.

4.3 The Scan Mode

The antenna used in the scanning involves three operational modes, which include:

1. Planar scan mode. A complete scan is performed along the horizontal (x-axis) direction in front of the object that is to be detected. Figure 4.3.1 shows the geometrical setup for this simple method, which involves a discrete scanning process, with a fixed spacing between samples. A total number of samples in a single planar scan refer to n. The planar scan method, however, cannot provide the exact shape of the front end of the object unless the normal direction is along the z-axis for every position, i.e. the object has a flat surface. However, this method can be used to detect the front surface of the object.

Object

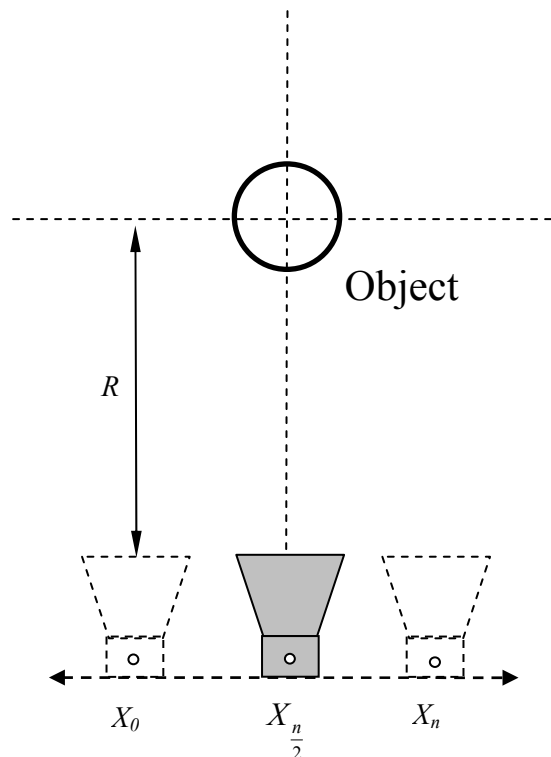R

X_0 $X_{\frac{n}{2}}$ X_n

Figure 4.3.1 The experiment setup for planar scan mode

2. Rotational scan mode. This is a more advanced method where the scanning is done while the object is rotated on a platform and fixed probe, as displayed in Figure 4.3.2. This process is equivalent to scanning around a static object. It uses a fixed number of rotation steps, for which the cylindrical rotation index, referred to as i throughout the paper, takes integer values ranging from 1 to 360 degrees.
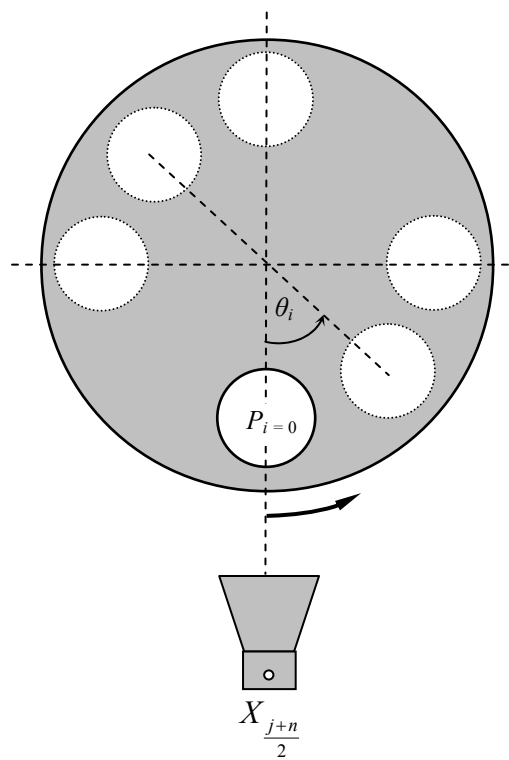

Figure 4.3.2 The experiment setup for rotational scan mode

3. Combined scan mode. This mode is a combination of the two previous ones, and produces results as if the scanning is done with multiple probes placed around the target. Since only one probe is used for the whole experiment, this method is called Single-Probe Detection and Reconstruction (SPIDR) technique. For each angle of rotation, a complete planar scan is performed. Figure 4.3.3 shows the way the object is rotated on the platform. The planar scan operation used in this mode is referred to as Combined Planar Scan (CPS). For every single rotational step, a planar scan is performed
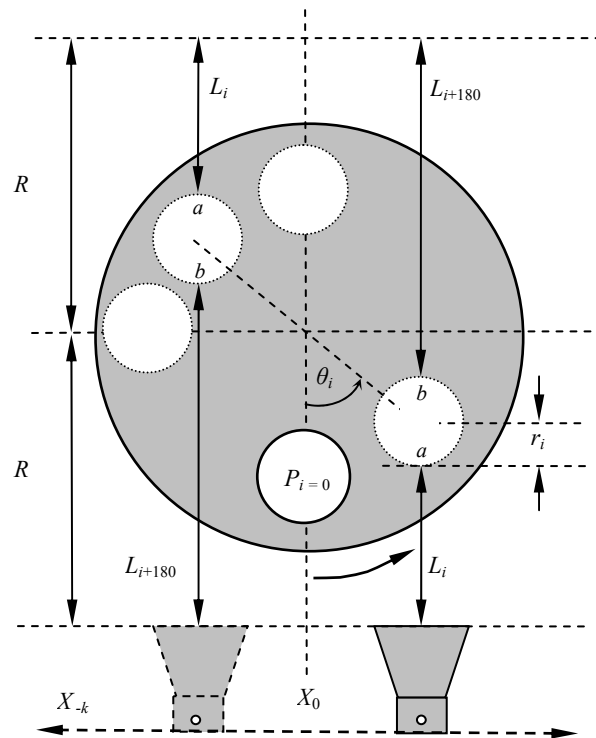

Figure 4.3.3 The experiment setup for cylindrical scan mode

All three methods are based on sending a pulse in the $+z$ direction at every scanning step, after which the reflected signal is recorded and stored for future processing. The electromagnetic wave arrives at the surface of the object with a given polarization to minimize signal loss and the amount of reflection and transmission at that interface depends, among other factors, on; i) the constitutive parameters of the two media that form the interface, ii) the angle of incidence of the oblique incidence wave. Since, for non-ferromagnetic materials, a perpendicularly polarized wave will not have total transmission, this is the polarization of choice for a scan and the horn antenna should be oriented accordingly. Given that the reflected wave depends on the surface contour of the target (Figure.4.3.4), a zero-degree (or near zero) angle of incidence ensures a maximum reflection entering the probe.
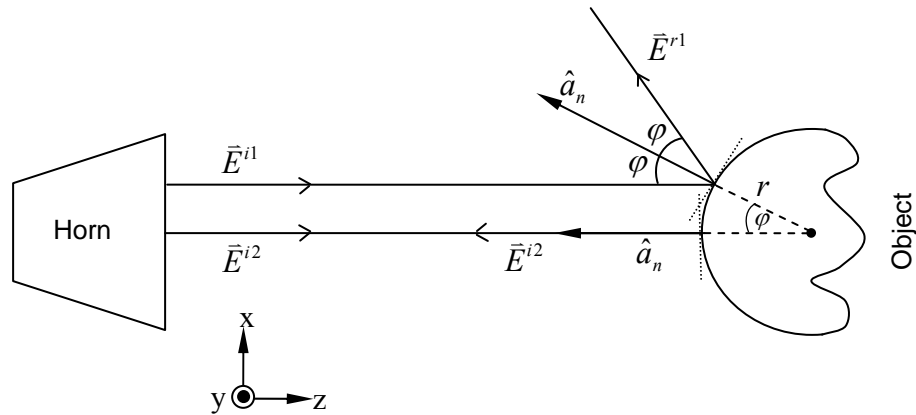

Figure 4.3.4 Probe and object configuration

Also, an object detection and reconstruction requires a cylindrical or combined scanning mode because in the rotational mode there is always an angle of rotation at which the normal to the interface is parallel to the direction of the incident wave. The linear scan in this mode is used for the detection of the object. However, if the object is round-shaped, the maximum amplitude of the reflected wave gives the location of its center since all other values will correspond either to waves reflected from different angles of incidence (not normal to the surface of the object) or waves missing the object.

The antenna, object and plastic container setup is illustrated in Figure 4.3.5
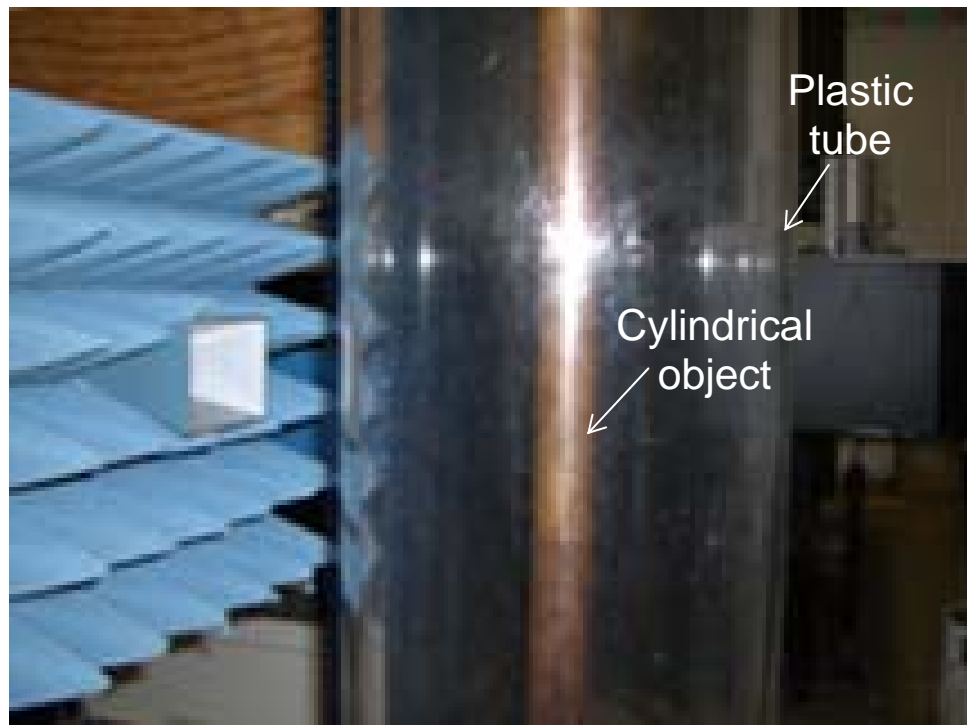

Fig. 4.3.5 Experiment setup

4.4 Measurement Procedure

The scanner system is controlled by a PC controller. The measuring operation is processed by PC recorder and the measurement includes the following steps

1) Specification of the area to be scanned in the XY plane including spacing steps in the X direction for Planar scan mode and angular index of the rotational positioner for Rotational scan mode and Cylindrical scan mode.

2) At each specified X-Y location, the PC controller triggers the source in the Vector Network Analyzer and 50 to 800 (depending on specifications) measurement points of the two-port are done over the frequency band of interest which is 8.2 to 12.4 GHz. After the frequency domain measurements of S-parameters are completed, they are immediately converted to the time domain by VNA. The technique using for the conversion is inverse chirp Z transform. If necessary, this stage may also involve gating of undesired reflections using the various types of windows that can be set by the Gate function of the VNA.

3) Having obtained the data of S_{11} in time domain for a given location, the results are stored in the PC and the probe is moved to a new position and the measurement procedure is repeated.

4.5 Experimental Arrangement and NSI Parameters Setup

The measurement using the NSI system is divided into two stages: S-parameter in term of frequency domain with object present inside the plastic container, and the attenuation measurement which is no object present. The results of these measurements are explained in chapter 4.

The system component for NSI system setup can be observed in Figure 4.5.1. Since only 1 probe is used for the whole experiment, S – parameter which is S_{11} at port 1 will be observed.
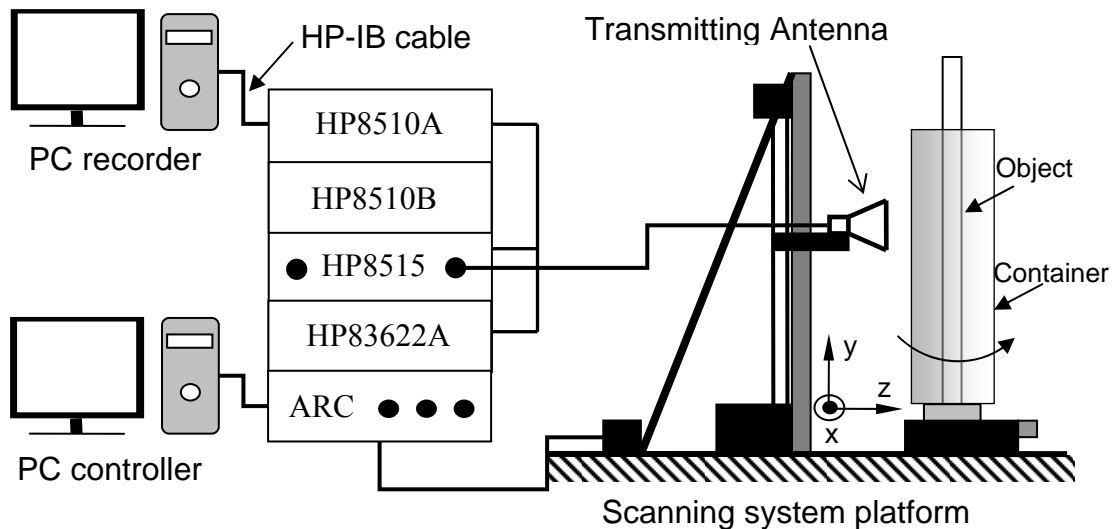

Figure 4.5.1 Experimental configuration

4.6 Antenna Characteristics and Simulation Configuration

In this section, we will discuss on electromagnetic field simulation software and configuration. The software we use is Computer Simulation Technology (CST) Microwave Studio 5. This software is a fully featured software package for electromagnetic analysis and design in the microwave frequency range. The structure can be easily designed by using solid modeling front-end function which is based on ACIS modeling kernel.

The pyramidal horn is widely used as a standard to make gain measurement of other antennas. It is often referred to as a standard gain horn. In order to design a pyramidal horn, there are some equations related to the desired gain and the dimension a, b of the rectangular feed waveguide which is shown in Figure 4.6.1. The objective of the design is to determine the remaining dimensions (a_1, b_1, p_e, p_h, P_e, and P_h) that will lead to an optimum gain. The gain of the antenna can be related to its physical area by

$$G_0 = \frac{4\pi}{2\lambda^2}(a_1 b_1) = \frac{2\pi}{\lambda^2}\sqrt{3\lambda\rho_h}\sqrt{2\lambda\rho_e} \tag{4.1}$$

For a pyramidal horn to be physically realizable, P_e, and P_h of

$$P_e = (b_1 - b)\left[\left(\frac{\rho_e}{b_1}\right)^2 - \frac{1}{4}\right]^{1/2} \tag{4.2}$$

$$P_h = (a_1 - a)\left[\left(\frac{\rho_h}{a_1}\right)^2 - \frac{1}{4}\right]^{1/2} \tag{4.3}$$

must be equal. Using this equality, it can be shown that (4-1) reduces to

$$\left(\sqrt{2X} - \frac{b}{\lambda} \right)^2 (2X - 1) = \left(\frac{G_0}{2\pi} \sqrt{\frac{3}{2\pi}} \frac{1}{\sqrt{X}} - \frac{a}{\lambda} \right)^2 \left(\frac{G_0^2}{6\pi^3} \frac{1}{X} - 1 \right) \tag{4.4}$$

where

$$\frac{\rho_e}{\lambda} = X \tag{4.5a}$$

$$\frac{\rho_h}{\lambda} = \frac{G_0^2}{8\pi^3} \left(\frac{1}{X} \right) \tag{4.5b}$$

Equation (4-4) is the horn-design equation. As the first step of the design, we have to find the value of X which satisfies (4-4) for a desired gain G_0 (dimensionless). Using an iterative technique, the value of X will be equal to 11.38 and next step we need to determine p_e and p_h using (4-5a) and (4-5b), respectively. Find the corresponding values of a_1 and b_1 using

$$a_1 = \sqrt{3\lambda\rho_h} \tag{4.6}$$

$$b_1 = \sqrt{2\lambda\rho_e} \tag{4.7}$$

The value of P_e and P_h can be determined by using (4-2) and (4-3), respectively.
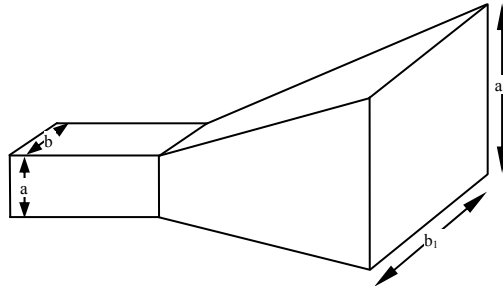

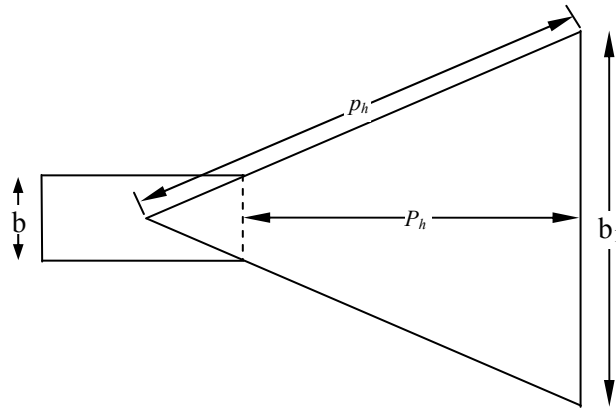Figure 4.6.1 Pyramidal horn and coordinate system
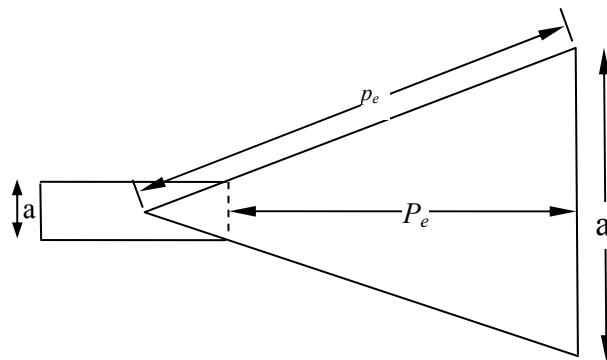

Figure 4.6.2 E-plane view

Figure 4.6.3 H-plane view

The structure design will use the information supplied in Table 4.6.1

Table 4.6.1 Antenna and object parameter

Probe Parameters	Parameter Value	Object Parameters	Parameter Value
Gain (G_0)	22.6 dB.	Radius (r)	0.65 cm.
Waveguide height(a)	0.95 cm.	Height (h)	5.00 cm.
Waveguide width (b)	2.22 cm.		
Aperture height (a_1)	5.39 cm.		
Aperture width (b_1)	7.30 cm.		
Taper (p_e)	13.08 cm.		
Taper (p_h)	10.79 cm.		
P_e	8.87 cm.		
P_h	8.60 cm.		

CST Microwave Studio provides the function of the structure design and electromagnetic field simulation. The pyramidal horn antenna can be constructed with the parameter obtained. The material of pyramidal horn design is perfect electric conductor (PEC). The horn is placed horizontally which mean E-field vector is oriented in y-direction and the electromagnetic wave propagates to z-direction as shown in Figure 4.6.4
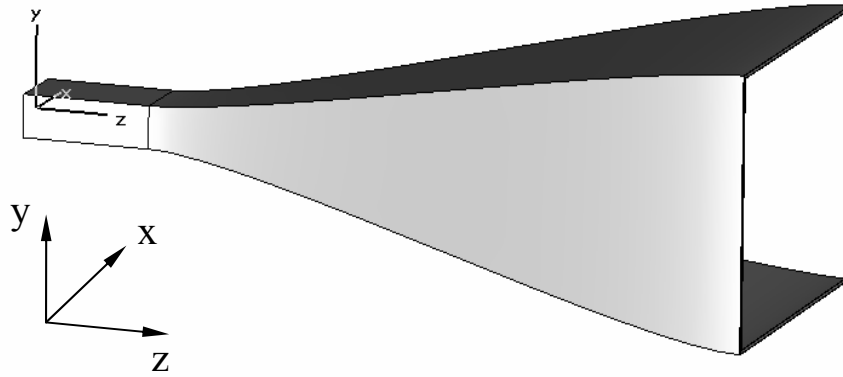
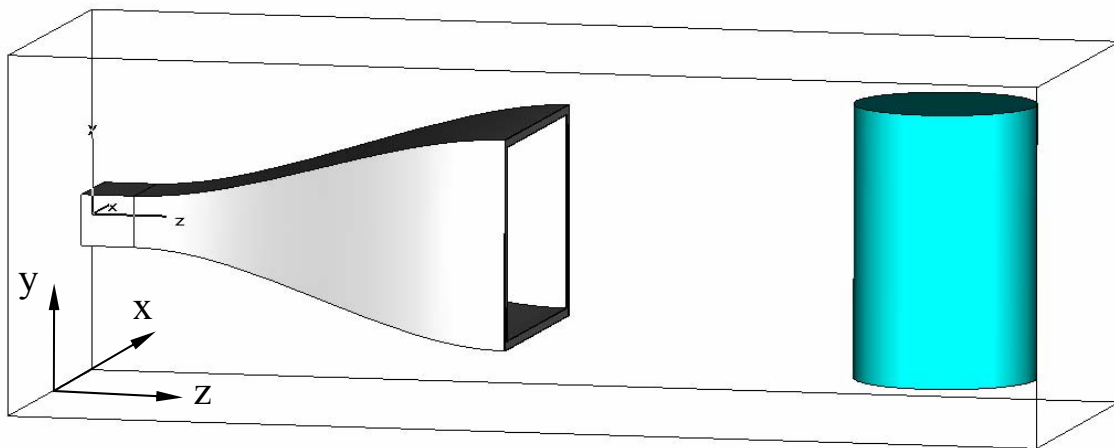Figure 4.6.4 Pyramidal horn antenna profile

Figure 4.6.5 Pyramidal horn antenna and target configuration

The next step is to apply waveguide port into opened-end of the waveguide structure and defining the direction of the wave propagation which is *z*-direction as shown in Figure 4.6.5. Also apply the excitation pulse which is Gaussian pulse into the waveguide port. Figure 4.6.6 (a) and (b) show two different methods to apply boundary condition. The former is the method for a symmetrical structure. We can define the boundary condition covering only ¼ of the structure as shown in Figure 4.6.6 (a). The latter is for any structure profile. For this method, we define zero *E*-field at the boundaries which are parallel to *xy* plane and *xz* plane and also define zero H-field at the boundaries which is parallel to *yz* plane. These mean that we apply absorbing condition around the entire structure as shown in Figure 4.6.6 (b). The main different between these methods is simulation time consuming. If the boundary condition is applied for symmetry object, the simulation will take less than ¼ times that of asymmetrical structure.
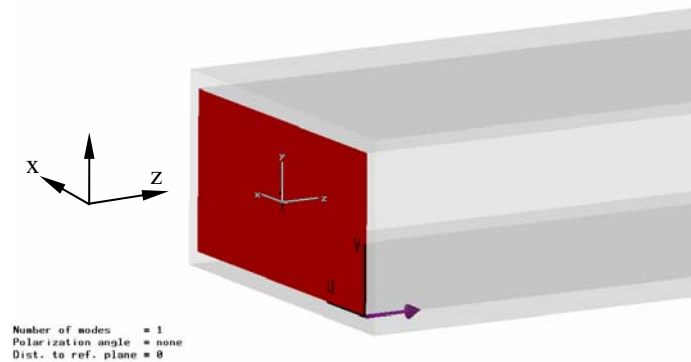

Number of modes   = 1
Polarization angle = none
Dist. to ref. plane = 0

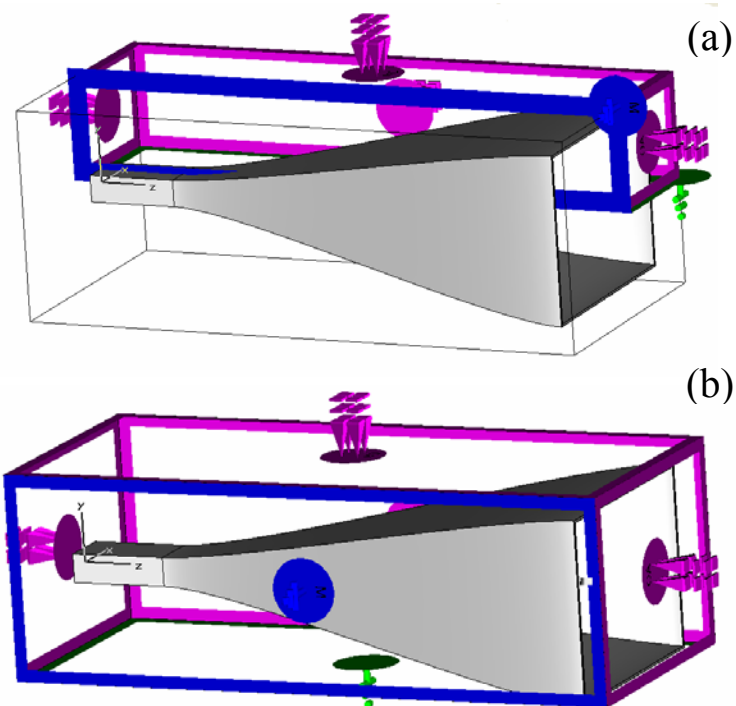Figure 4.6.6 Waveguide port configuration

(a)

(b)

Figure 4.6.7 Boundary conditions

The antenna characteristics, results from the simulation setup and reconstructed image using the techniques are described. The CST software calculated gain pattern at frequency 10.3 GHz, the antenna has gain of 21.04 dB. Figure 4.6.7 shows antenna gain result in Cartesian coordinate system.
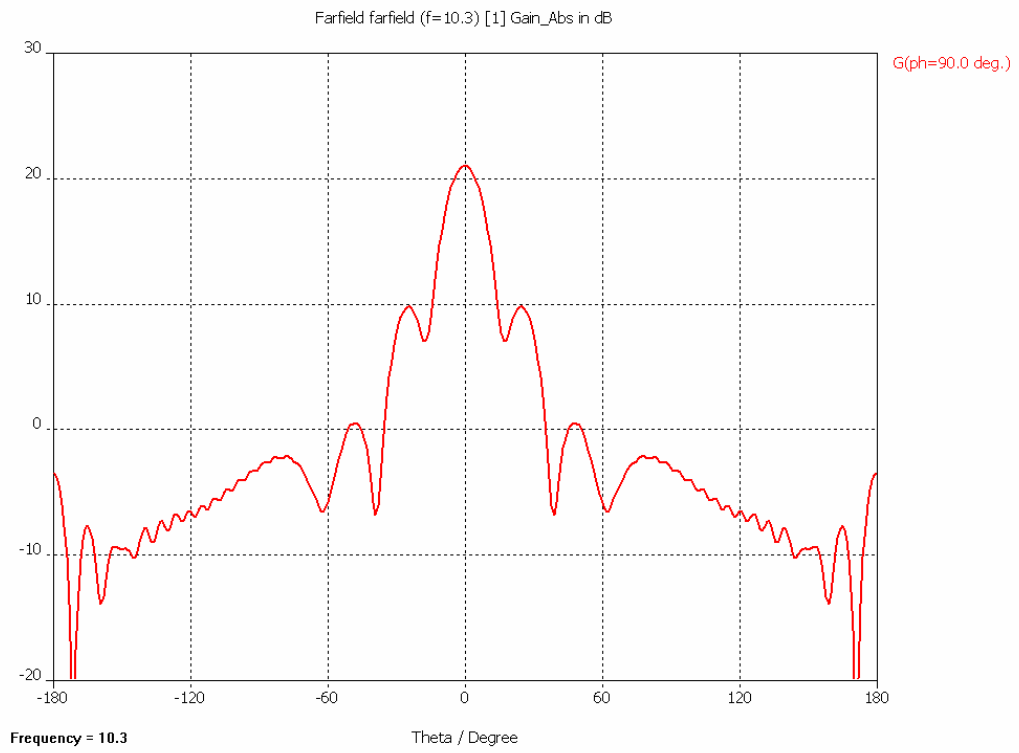
Figure 4.6.8 Pyramidal horn antenna gain result in far-field region

The pattern behavior of the E-field simulation in far-field region on pyramidal horn antenna is illustrated by Figure 4.6.8.


```
Type          = Farfield
Approximation = enabled (kR >> 1)
Monitor       = farfield (f=10.3) [1]
Component     = Abs
Output        = Gain
Frequency     = 10.3
Rad. effic.   = 0.9946
Tot. effic.   = 0.9903
Gain          =  21.04 dB
```
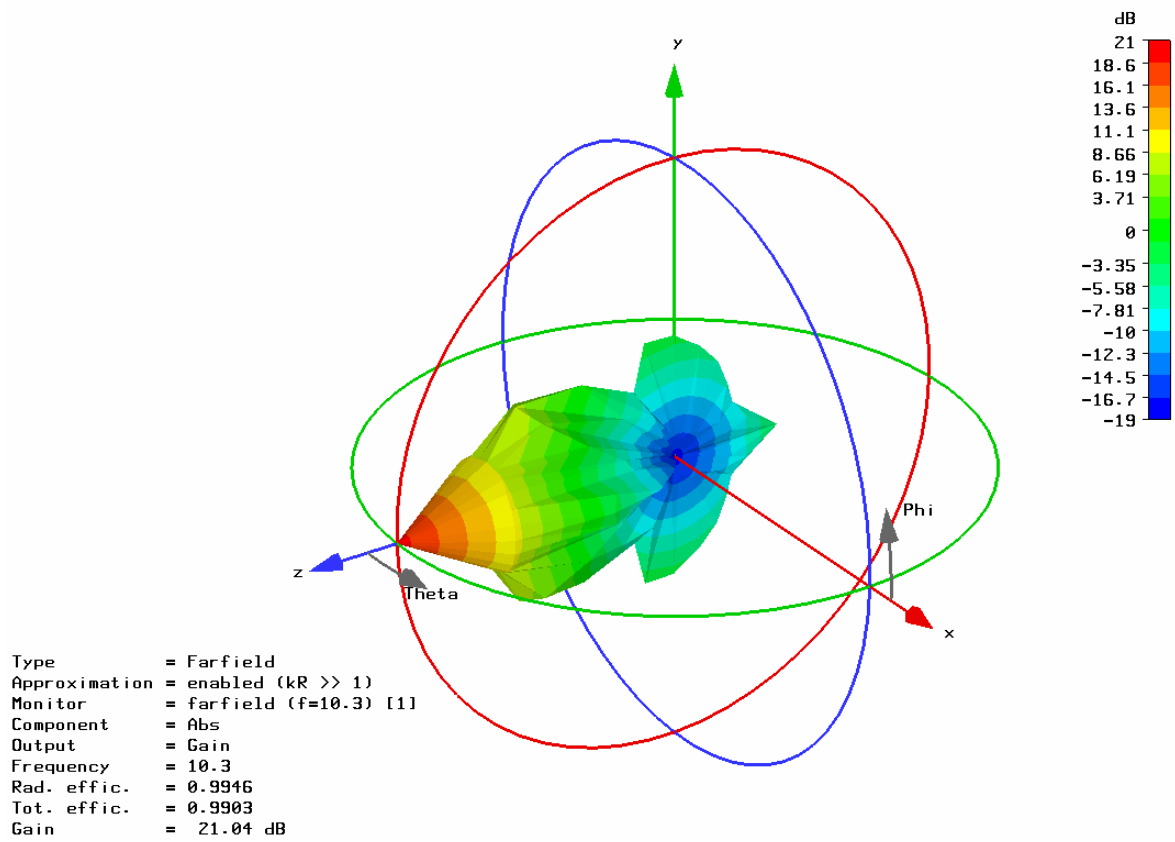
Figure 4.6.9 Radiation pattern of pyramidal horn antenna in far-field

Chapter 5: Simulation and Experimental Results

5.1 Simulation Results

Figure 5.1.1 (a) and (b) show S_{11} magnitude (dB) and phase (degree) results in frequency domain for the reflections obtained from the object. The results are measured by placing an object in front of the probe as shown in Figure 5.3.1.
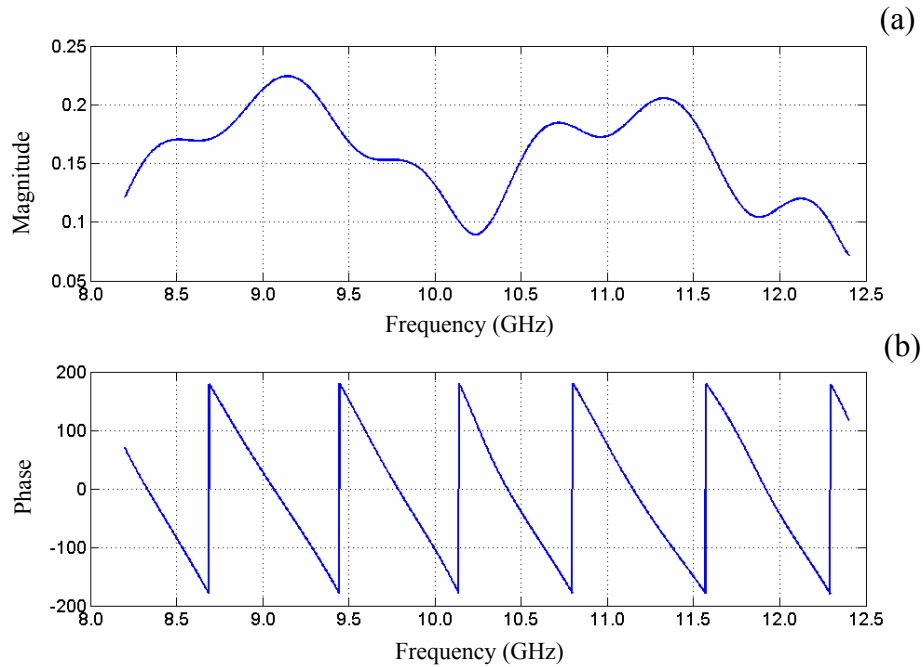
(a)

(b)

Figure 5.1.1 *S*-parameter results in frequency domain: (a) magnitude and (b) phase response

Since the objective is to accurately determine the distance of the reflecting surface from the probe, this distance is calculated by measuring the time-domain scattering parameter S_{11} for every sample:

$$S_{11} = \Gamma_0 e^{-j2\beta l},\qquad (5.1.1)$$

where Γ_0 is a ratio of the reflected wave from the object and the incident wave from the antenna, β is the phase constant, and l is the distance from the probe to the object at every step of the scanning process.

In order to obtain the corresponding *S*-parameter in term of time domain, Inverse Fast Fourier Transform will be applied [27]. Figure 5.1.2 shows S_{11} results in time domain which is associated with the frequency domain results from Figure 5.1.1. The peak result in Figure 5.1.2 represents the round-trip measured time delay from the probe to the object. The corresponding distance from the probe to the object can be determined by using

$$d = \frac{\tau \cdot c}{2\sqrt{\varepsilon_r}} \tag{5.1.2}$$

where *d* is the distance from the probe to the object, τ is the measured time delay, *c* is speed of light.
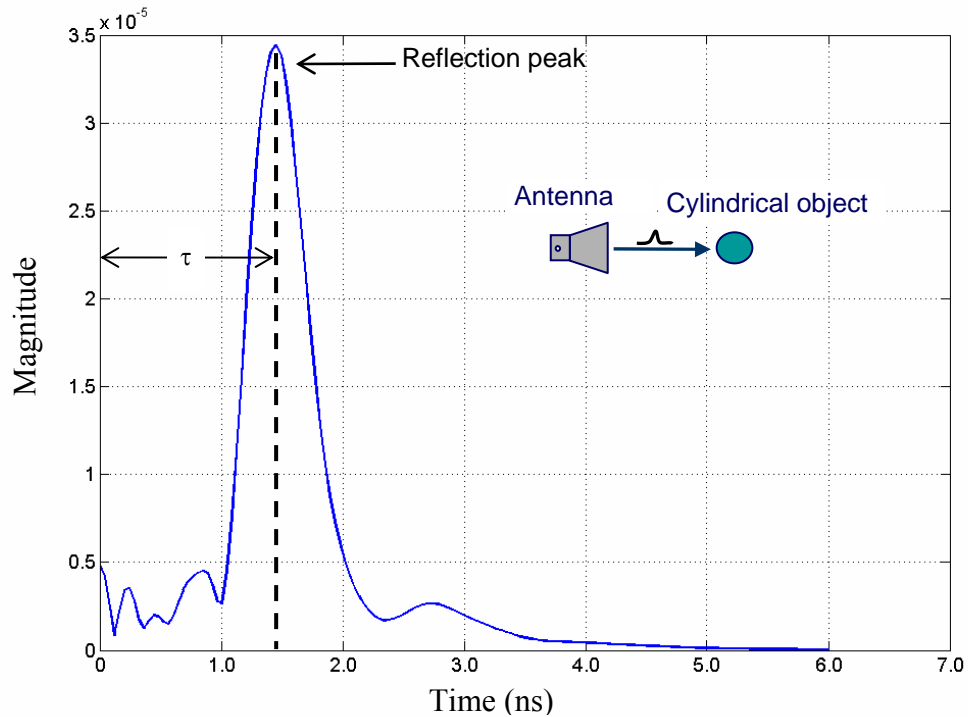

Figure 5.1.2 *S*-parameter result in time domain

5.2 Calibration Procedure

The reflected signal theoretically consists of signal reflected by the coaxial cable, waveguide connector, plastic container, and object as shown in Figure 5.2.1. This relation is described by the average value by

$$S_{reflected} = S_{cable} + S_{waveguide} + S_{container} + S_{object} \qquad (5.2.1)$$

The reflected signal from the object can be obtained by subtracting the reflected by coaxial cable, waveguide connector, and plastic container from the total reflected signal. The reflected by coaxial cable, waveguide connector, and plastic container can be obtained by measuring the plastic container signal with no presence of the object in the container which is filled with air. The measurement setup is just the same as it is illustrated in Figure 3.1.2 but with no presence of the object in the container. Figure 5.2.2 illustrates S_{11} signal measured with no object in the container. There are also 2 reflection peaks from 2 sides of the plastic container. This value is measured when the probe is placed at X_0 position (Figure 4.3.1).
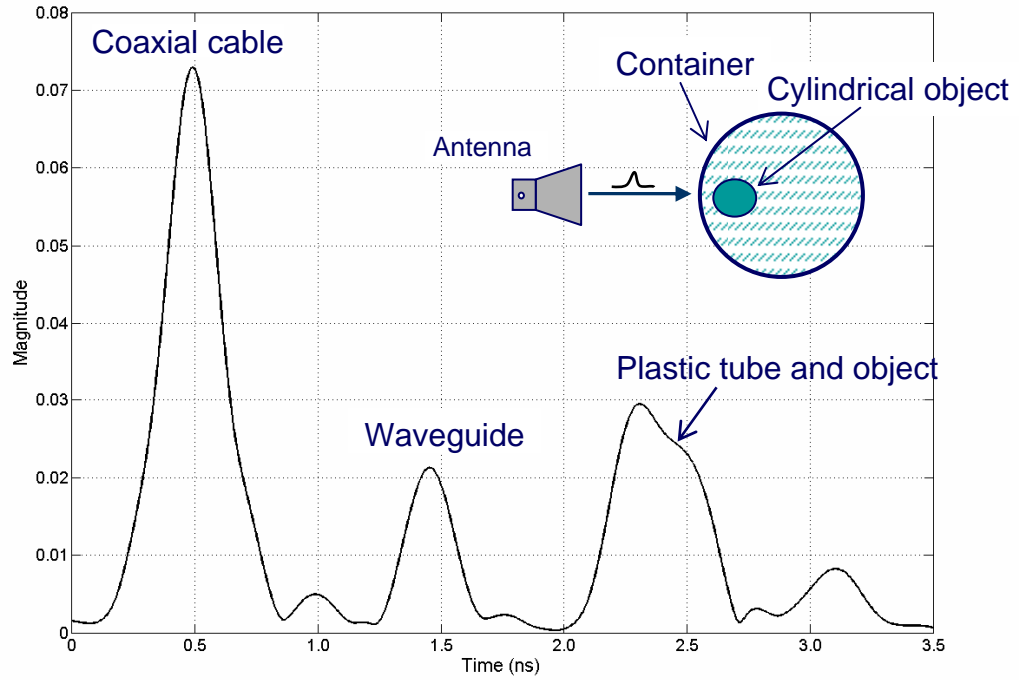
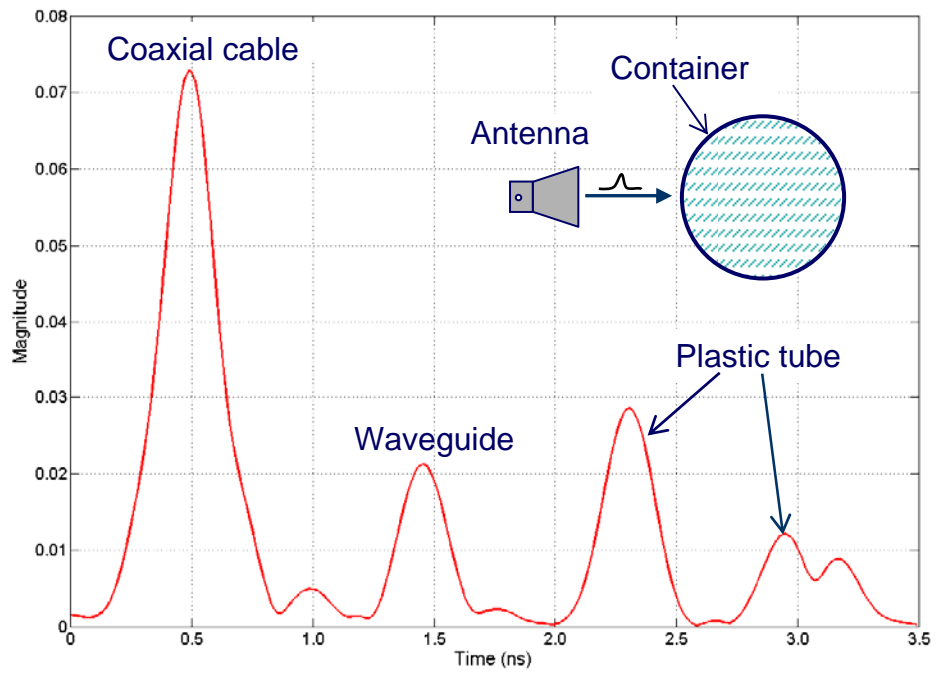Figure 5.2.1 S_{11} signal result with object present

Figure 5.2.2 S_{11} signal result with no object present

The subtracting method is illustrated in Figure 5.2.3. It shows the pre-calibrated signal from Figure 5.2.1, the calibrating signal from Figure 5.2.2, and calibrated signal which is the blue line with marker. The calibrating signal was obtained from the reflection result without the presence of object inside the container. By subtracting the pre-calibrated signal with the calibrating signal, the reflection from the object will be obtained from the calibrated signal.
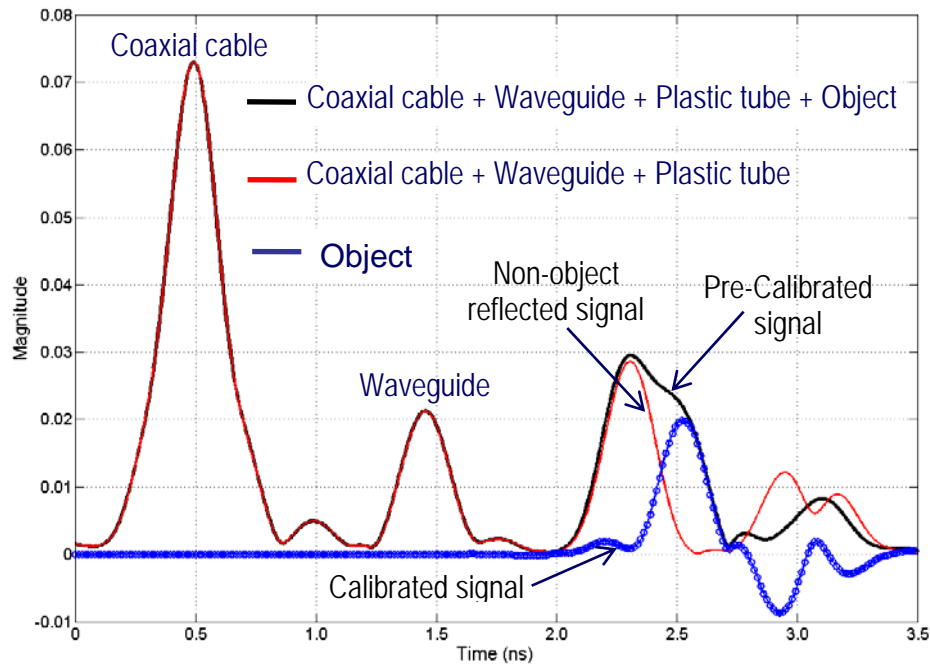
Figure 5.2.3 S_{11} signal result in time domain before and after subtraction method.

After scan performing and data recording, S_{11} signal which is the ratio of the reflected wave from the object and the incident wave from the antenna will be used to determine the corresponding distance from the probe to the object by using (5.1.1).

5.3 Single Probe Imaging through Detection and Reconstruction (SPIDR) Algorithm

The object detection and shape reconstruction algorithm for SPIDR method is shown in Figure 5.3.1

Figure 5.3.1 Image reconstruction algorithm for SPIDR method.

5.4 Experimental Results

5.4.1 Planar Scan Mode
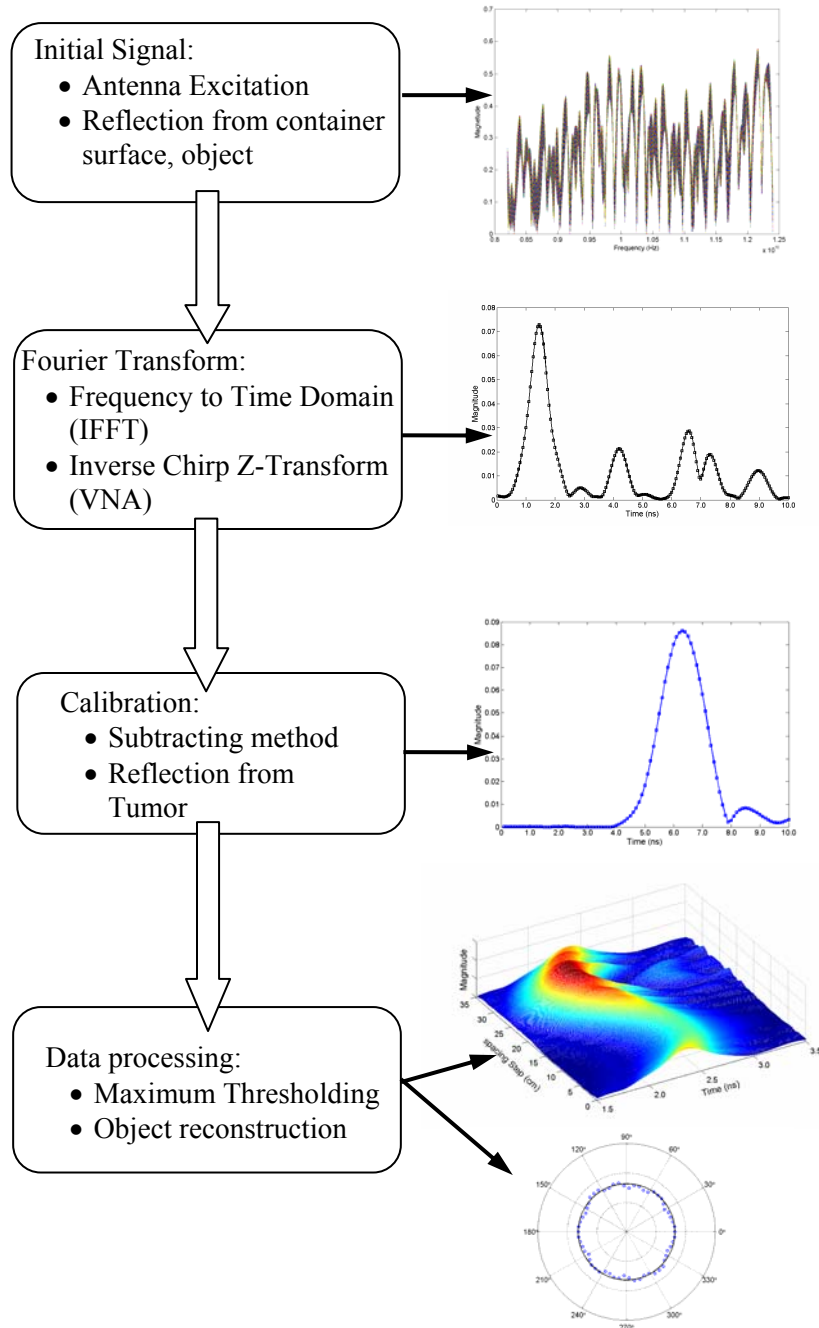
Fig. 5.4.1.1 (a) and (b) show the time-domain results for the reflections obtained from the object using conventional planar scan mode before and after calibration method, respectively. This mode is performed by scanning the probe along X-axis while 1000 data points of S_{11} in time domain are recorded with the spacing of 0.05 cm. The reflections from the waveguide and coaxial cable have been subtracted in the reconstruction phase. This scan mode can be used to locate an embedded object as shown in Fig. 5.4.1.2. However, this approach is only valid for the case of normal incidence; otherwise, this distance will be slightly distorted and should be somehow corrected. The problem here is that the angle of incidence (φ) is not known. For each scanning position, i.e., from X_{-k} to X_{+k}, the time at which S_{11} has maximum amplitude gives some value of the round-trip delay experienced by the pulse which may give the impression that the object is further away since the reflected wave will travel with more distance of $r - r.cos(\varphi)$, where r is the object radius. This distance can be approximated to be almost equal to d for small values of φ, i.e., the X_0 position in Fig. 1. Consequently, even if the computed distance is not accurate, there is reflection at that point which means the object is there.
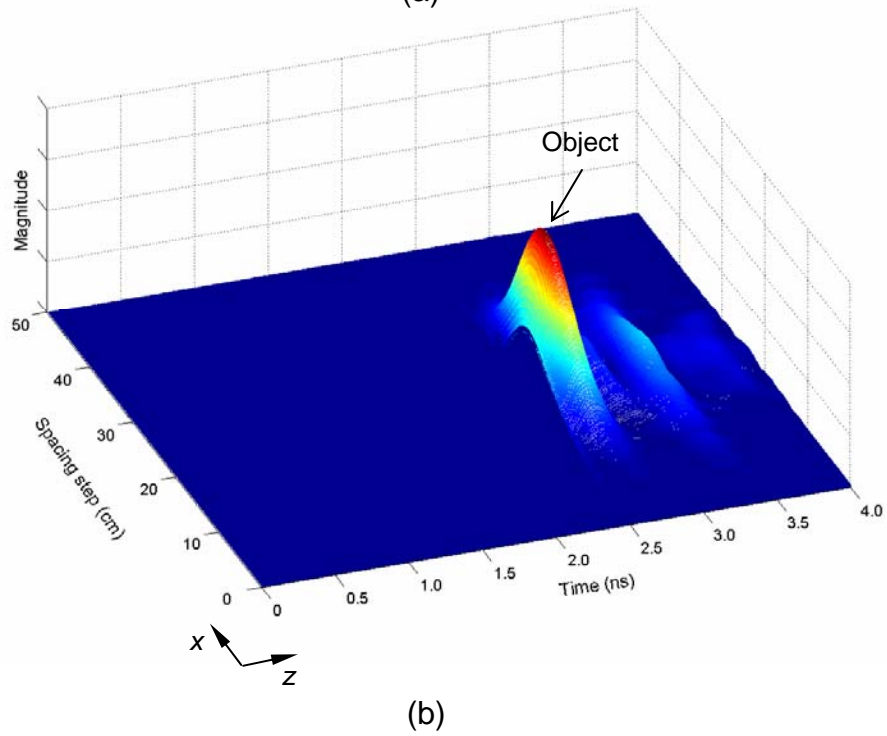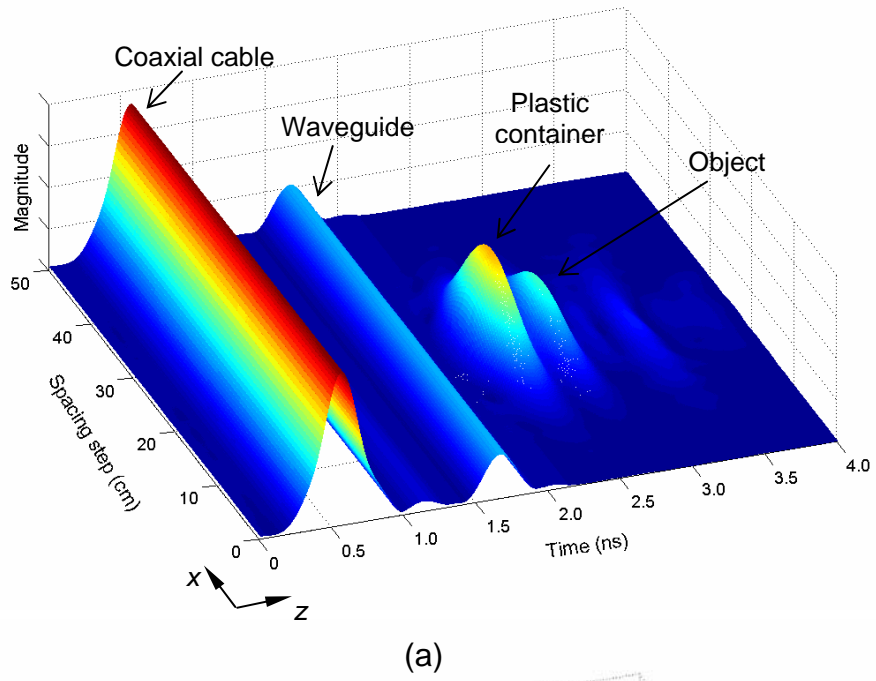
Figure 5.4.1.1 *S*-parameter results of the planar scan mode in time domain
(a) before and (b) after calibration

The planar scan can provide the object front-surface detection. The embedded object location can be shown in Cartesian coordinate system as shown in Figure 5.4.1.2.
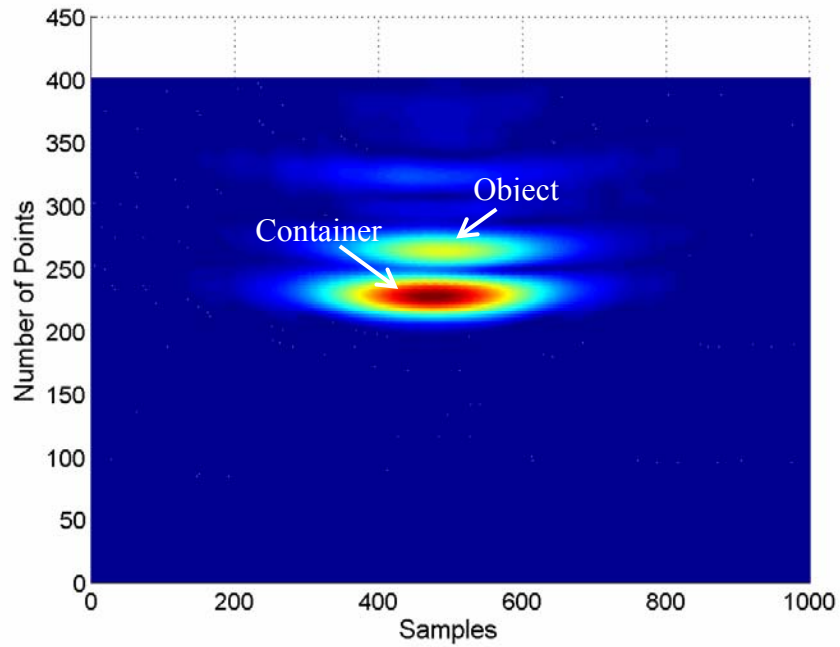

Figure 5.4.1.2 Front surface reflection from plastic container and object

5.4.2 Rotational Scan Mode

This mode is performed by fixing the probe at X_0 while 360 samples of S_{11} in time domain are recorded with a one degree incremental rotation step from 1° to 360°. The reflections from the waveguide and coaxial cable have been subtracted in the reconstruction phase. The results of S_{11} in time domain can be shown in Fig. 5.4.2.1 (a) and (b) before and after calibration, respectively. The data obtained from this scan mode can only be achieved when the embedded object is located within the rectangular waveguide width. Otherwise, there is no signal reflected back from the target to the waveguide. Figure 5.4.2.2 (a) and (b) shows S_{11} results from the rotational scan mode in time domain when the object is placed within and out of radiation beamwidth, respectively. However, this limitation is solved by using the CS mode, which provides object reconstruction regardless of its location on the platform.
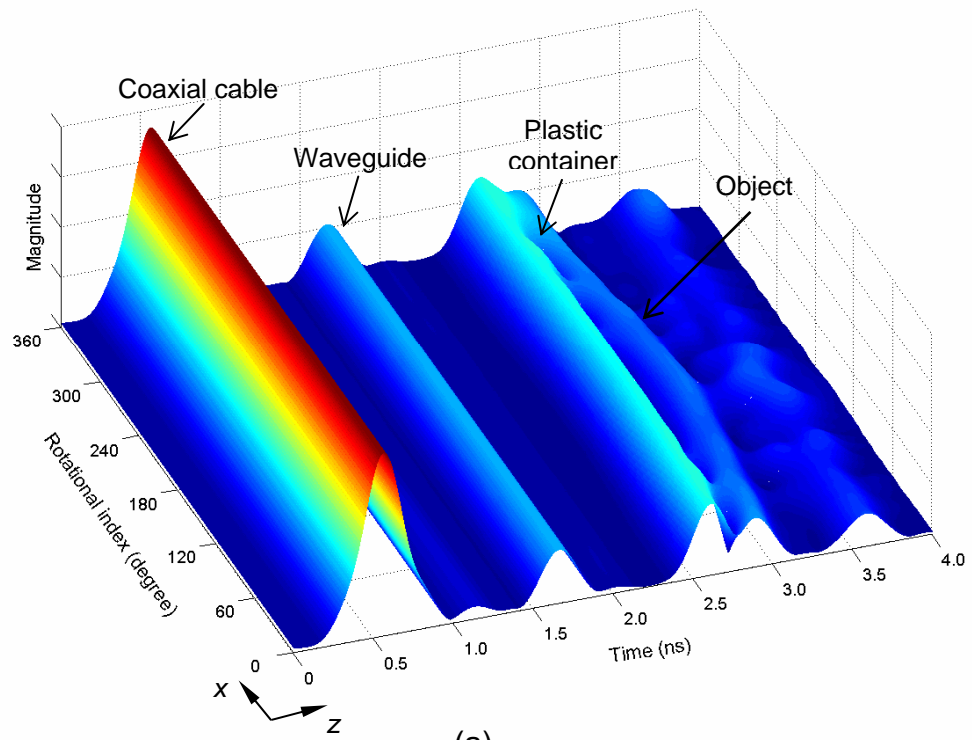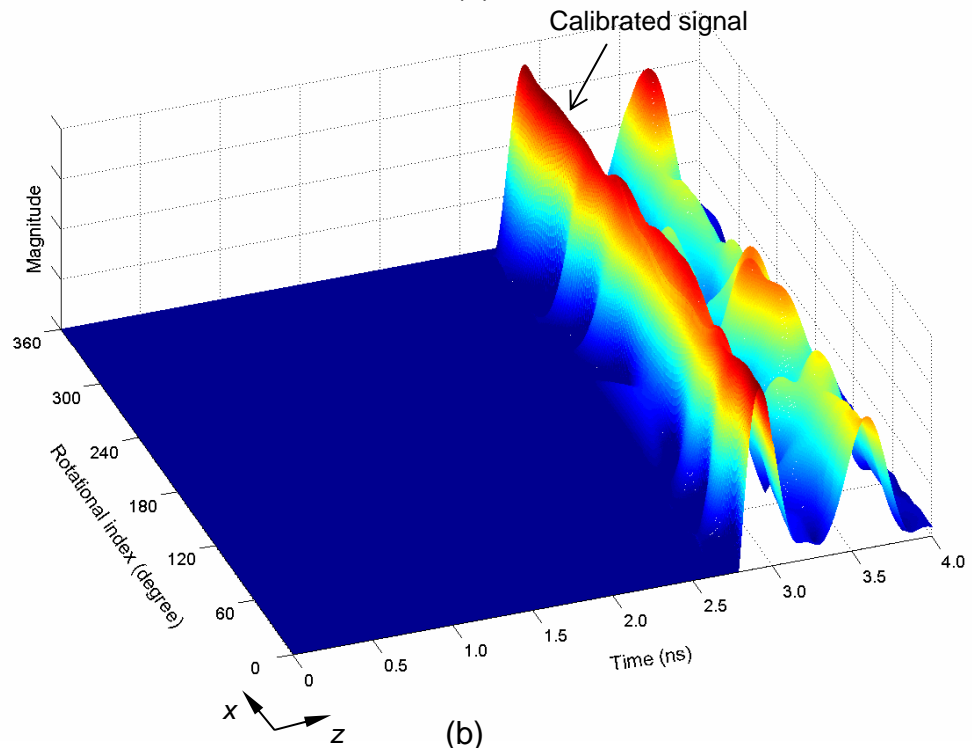
Figure 5.4.2.1 S_{11} results of the rotational scan mode in time domain (a) before and (b) after calibration

Figure 5.4.2.2 S_{11} results of the rotational scan mode in time domain when the object is placed (a) within and (b) out of the radiation beamwidth

5.4.3 Combined Scan Mode

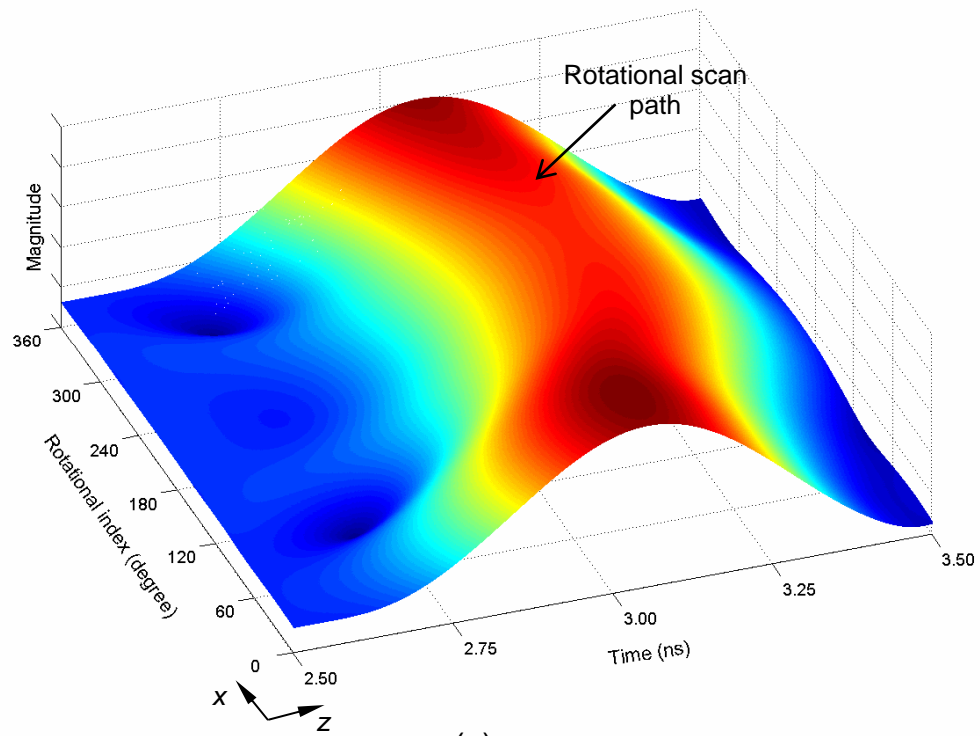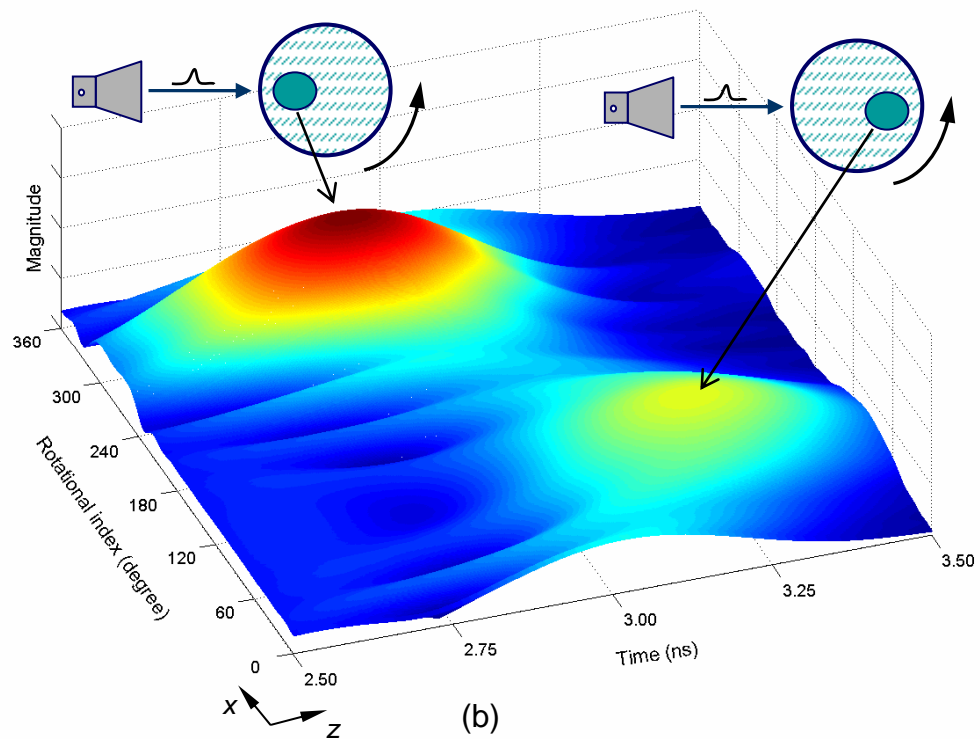This mode is a combination of planar and rotational scan modes. In this experiment, for each CS step, i.e., a one degree incremental rotational step from 1° to 360° and a 0.5 mm incremental spatial step of a total length of 20 cm. from X_{-k} to X_{+k}, the time-domain S_{11} values for a total of 801 points were measured. In the calibration stage, the reflected signal from the object can be obtained by subtracting the signal with the reflections from the waveguide, coaxial cable, and the container as previously described. The total of $360 \times 40 \times 801$ (= 11534400) calibrated data points as shown in Figure 5.4.3.1 (a) were arranged in a supermatrix form as given by

$$A_{(i,j)} = \begin{bmatrix} \left[B_{(1,1)} \right] & & \\ & \ddots & \\ & & \left[B_{(i,j)} \right] \end{bmatrix}_{(360,40)},$$

(5.4.3.1)

where

$$B_{(i,j)} = [S_{11}(0) \cdots S_{11}(800)]_{(1,801)}$$

(5.4.3.2)

is the S_{11} vector with a dimension of 801, i is the rotational angle index, i.e., 360 and j is planar spatial index, i.e., 40. After the subtracting calibration and data arrangement, the maximum peak of S_{11} corresponding to the distance d between the probe and the object was determined through

$$B'_{(i,j)} = \max(B_{(i,j)}).$$

(5.4.3.3)

The matrix $A'_{(i,j)}$ whose elements are chosen from the matrix A through (5.4.3.3) and shown in Figure 5.4.3.2 can be expressed as

$$A'_{(i,j)} = \begin{bmatrix} B'_{(1,1)} & & \\ & \ddots & \\ & & B'_{(i,j)} \end{bmatrix}_{(360,40)}.$$
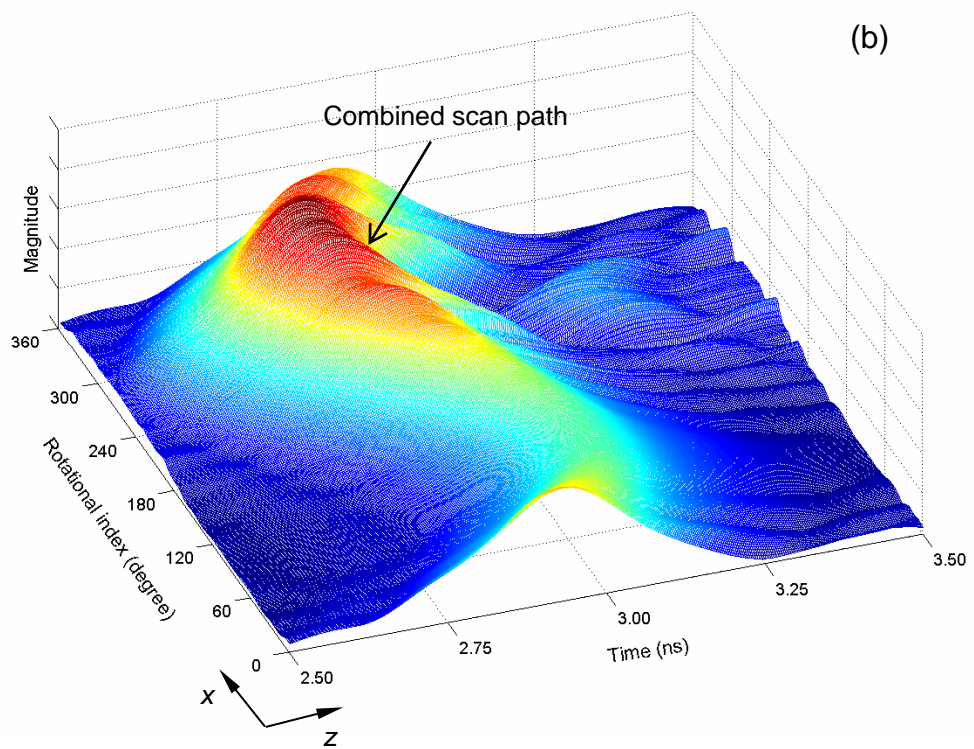
(5.4.3.4)
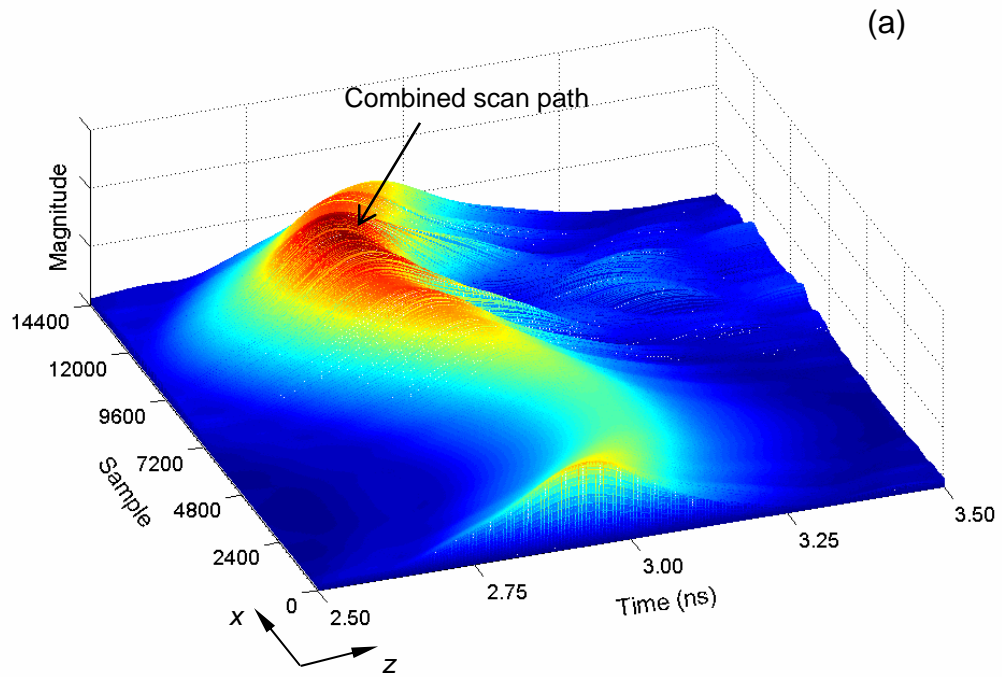
Figure 5.4.3.1 *S*-parameter results of the combined scan mode in time domain (a) before and (b) after data thresholding

Next, to obtain the reflection with a near-zero angle of incidence for each rotational step, the data in each row of (5.4.3.4) with a maximum value was chosen through

$$B''_{(i)} = \max[B'_{(i,1)} \cdots B'_{(i,j)}].$$ (5.4.3.5)

The resulting vector A'' with elements obtained from (5.4.3.57) can be given by the matrix

$$A'' = \begin{bmatrix} B''_{(1)} \\ \vdots \\ B''_{(i)} \end{bmatrix},$$ (5.4.3.6)

where the elements are made use of a reconstruction of the object's surface contour. The data acquisition using the equations described above is demonstrated by the diagram shown in Fig. 5.4.3.2. The plot covers two consecutive rotational indices representing the values of the elements in the matrix A' after the maximum peak detection process of the input signals. In addition, the peak value of each rotational index represents each element in the vector A''. The reversal of the spatial step indices between each rotational index is resulted according to the hardware setup for a probe with a continuous movement, i.e., the probe moves from X_{-k} to X_{+k} for the rotational index i and simultaneously starts to move for the next rotational index $i+1$ from X_{+k} to X_{-k}. Figure 5.4.3.1 (b) shows the time domain result for the reflections obtained from the object after data thresholding and processing under application of the SPIDR method.
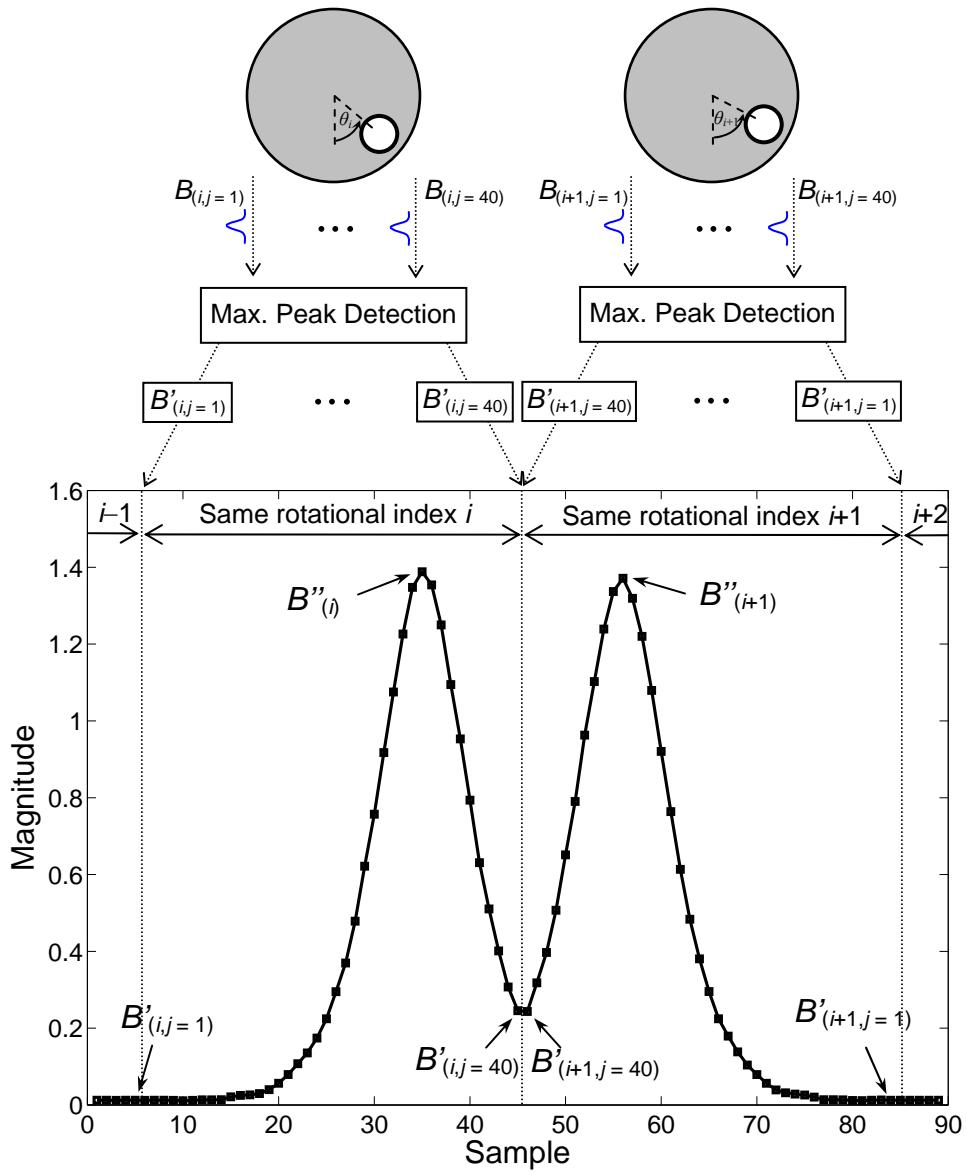
Figure 5.4.3.2 Data acquisition scheme.

5.5 Object Reconstruction Results

In the object-reconstruction stage, the vector A'' in (5.4.3.6) is used to determine the distance L from the probe to the object's front surface. For each rotational angle index, the distance can be computed by

$$L_i = \frac{B_i'' \bullet c}{2\sqrt{\varepsilon_r}} \; .$$ (5.5.1)

The radius of the embedded object can be determined using

$$r_i = R - \frac{L_i + L_{i+180}}{2} \; ,$$ (5.5.2)

where r_i is the distance between the center of the object and the surface that is tangent to the incident wave, found at each angle of rotation, and R is the distance described in Figure 5.5.1. Using the radii for each angle of rotation found from (5.5.2) and using a polar coordinate system, the object can be reconstructed as shown in Figure 5.5.2. The solid line represents the actual object, the circle marker being the reconstructed object resulting from applying SPIDR method. The averaged radii determined from theoretical computation and experimental analyses are 0.62 and 0.66 cm, respectively, with an approximate 7 % error.
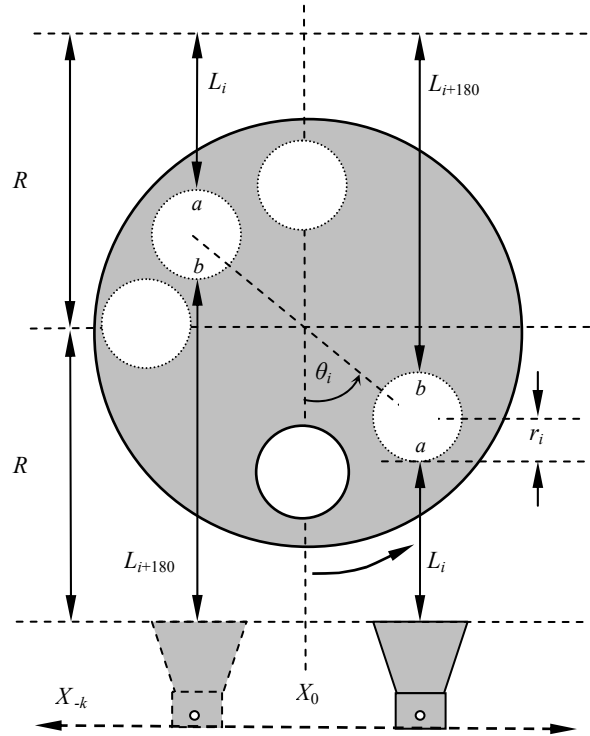
Figure 5.5.1 Reconstruction method scheme.

The SPIDR technique performing CS mode can be applied to detect and reconstruct an object which is embedded in a medium. The resolution result of this technique depends on how many point of rotational index taken. The more number of points of rotational index, the better resolution will be. Figure 5.5.3 shows the polar plot of reconstructed object with 30 points of rotational index.
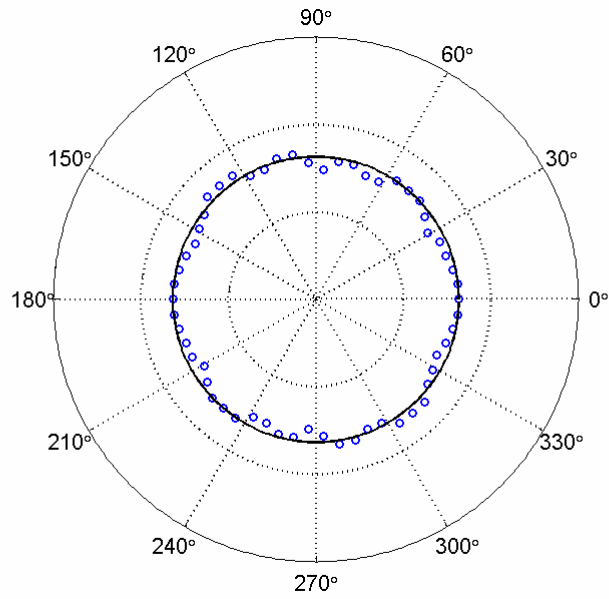
Figure 5.5.2 Polar plot of object radii for the reconstructed object (dashed line) and the actual object (solid line) with 60 points of rotational index.
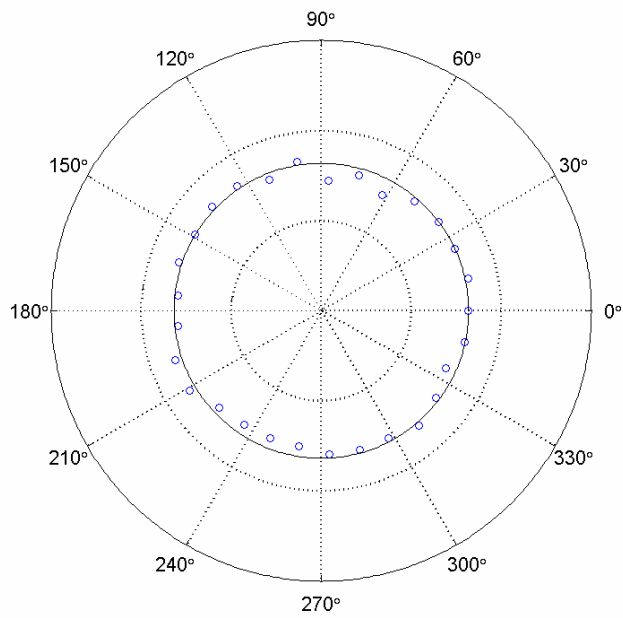
Figure 5.5.3 Polar plot of object radii for the reconstructed object (dashed line) and the actual object (solid line) with 30 points of rotational angle index.

Chapter 6: Conclusions and Future Work

There are many different techniques for the detection and reconstruction of the signal coming from an embedded object. The SPIDR technique described is a simple and accurate method for detecting and determining the distance of an embedded object which is later utilized for image reconstruction. The key in this reconstruction method is to accurately determine the distance of an object from a near field probe, which is extensively described in this work. The method takes into consideration the fact that the most accurate distance is the normal path between the probe and a point on the object that has almost zero reflection angles. It employs a frequency-synthesized pulse for scanning in the planar and cylindrical systems (described earlier) using a near-field antenna to identify the object.

The averaged radii of the object determined in this work through theoretical calculations and experiments are 0.62 and 0.66 cm, respectively, which has an approximate 7 % error. Thus the experimental results based on the SPIDR approach agree well with the simulations. The detection capability can be improved further through mechanisms that can discriminate and identify between such objects as cancerous and non-cancerous breast lumps which could make this method an important tool for breast cancer diagnostics and analysis.

The NSI system and the VNA used in the experiments have proven to be an important device that is capable of measuring antenna pattern and its characteristics even though the NSI software, HP8510, and HP 83622 are a little bit outdated. Still, the system is capable of measuring the pattern in both planar and cylindrical coordinate systems.

New and improved systems available today would further enhance the detection and reconstruction capability. Finally, the SPIDR technique using in this research is applicable to symmetrically embedded object. It is recommended that through further research, specifically through improvements in the detection and reconstruction method, non-symmetrically embedded object must be detected and reconstructed using the SPIDR technique, since most breast lumps are expected to be non-symmetric in shape.

MATLAB CODE (MC-I)

[OBJECT DETECTION FROM MEASURED DATA]

```
clc;
clear all;
CAL = dlmread('Scan10_1.dat',',',8,1);
T = dlmread('Scan10_1.dat',',',8,0);
Scan10_time = T(:,1);
Scan10_1 = dlmread('Scan10_1.dat',',',8,1);
Scan10_2 = dlmread('Scan10_2.dat',',',8,1);
Scan10_3 = dlmread('Scan10_3.dat',',',8,1);
Scan10_4 = dlmread('Scan10_4.dat',',',8,1);
Scan10_5 = dlmread('Scan10_5.dat',',',8,1);
Scan10_6 = dlmread('Scan10_6.dat',',',8,1);
Scan10_7 = dlmread('Scan10_7.dat',',',8,1);
Scan10_8 = dlmread('Scan10_8.dat',',',8,1);
Scan10_9 = dlmread('Scan10_9.dat',',',8,1);
Scan10_10 = dlmread('Scan10_10.dat',',',8,1);
Scan10_11 = dlmread('Scan10_11.dat',',',8,1);
Scan10_12 = dlmread('Scan10_12.dat',',',8,1);
Scan10_13 = dlmread('Scan10_13.dat',',',8,1);
Scan10_14 = dlmread('Scan10_14.dat',',',8,1);
Scan10_15 = dlmread('Scan10_15.dat',',',8,1);
Scan10_16 = dlmread('Scan10_16.dat',',',8,1);
Scan10_17 = dlmread('Scan10_17.dat',',',8,1);
Scan10_18 = dlmread('Scan10_18.dat',',',8,1);
Scan10_19 = dlmread('Scan10_19.dat',',',8,1);
Scan10_20 = dlmread('Scan10_20.dat',',',8,1);

Scan10_21 = dlmread('Scan10_21.dat',',',8,1);
Scan10_22 = dlmread('Scan10_22.dat',',',8,1);
Scan10_23 = dlmread('Scan10_23.dat',',',8,1);
Scan10_24 = dlmread('Scan10_24.dat',',',8,1);
Scan10_25 = dlmread('Scan10_25.dat',',',8,1);
Scan10_26 = dlmread('Scan10_26.dat',',',8,1);
Scan10_27 = dlmread('Scan10_27.dat',',',8,1);
Scan10_28 = dlmread('Scan10_28.dat',',',8,1);
Scan10_29 = dlmread('Scan10_29.dat',',',8,1);
Scan10_30 = dlmread('Scan10_30.dat',',',8,1);
Scan10_31 = dlmread('Scan10_31.dat',',',8,1);
Scan10_32 = dlmread('Scan10_32.dat',',',8,1);
Scan10_33 = dlmread('Scan10_33.dat',',',8,1);
Scan10_34 = dlmread('Scan10_34.dat',',',8,1);
Scan10_35 = dlmread('Scan10_35.dat',',',8,1);
```

```
Scan10_36 = dlmread('Scan10_36.dat',',',8,1);
Scan10_37 = dlmread('Scan10_37.dat',',',8,1);
Scan10_38 = dlmread('Scan10_38.dat',',',8,1);
Scan10_39 = dlmread('Scan10_39.dat',',',8,1);
Scan10_40 = dlmread('Scan10_40.dat',',',8,1);

Scan10_41 = dlmread('Scan10_41.dat',',',8,1);
Scan10_42 = dlmread('Scan10_42.dat',',',8,1);
Scan10_43 = dlmread('Scan10_43.dat',',',8,1);
Scan10_44 = dlmread('Scan10_44.dat',',',8,1);
Scan10_45 = dlmread('Scan10_45.dat',',',8,1);
Scan10_46 = dlmread('Scan10_46.dat',',',8,1);
Scan10_47 = dlmread('Scan10_47.dat',',',8,1);
Scan10_48 = dlmread('Scan10_48.dat',',',8,1);
Scan10_49 = dlmread('Scan10_49.dat',',',8,1);
Scan10_50 = dlmread('Scan10_50.dat',',',8,1);
Scan10_51 = dlmread('Scan10_51.dat',',',8,1);
Scan10_52 = dlmread('Scan10_52.dat',',',8,1);
Scan10_53 = dlmread('Scan10_53.dat',',',8,1);
Scan10_54 = dlmread('Scan10_54.dat',',',8,1);
Scan10_55 = dlmread('Scan10_55.dat',',',8,1);
Scan10_56 = dlmread('Scan10_56.dat',',',8,1);
Scan10_57 = dlmread('Scan10_57.dat',',',8,1);
Scan10_58 = dlmread('Scan10_58.dat',',',8,1);
Scan10_59 = dlmread('Scan10_59.dat',',',8,1);
Scan10_60 = dlmread('Scan10_60.dat',',',8,1);

Scan10_61 = dlmread('Scan10_61.dat',',',8,1);
Scan10_62 = dlmread('Scan10_62.dat',',',8,1);
Scan10_63 = dlmread('Scan10_63.dat',',',8,1);
Scan10_64 = dlmread('Scan10_64.dat',',',8,1);
Scan10_65 = dlmread('Scan10_65.dat',',',8,1);
Scan10_66 = dlmread('Scan10_66.dat',',',8,1);
Scan10_67 = dlmread('Scan10_67.dat',',',8,1);
Scan10_68 = dlmread('Scan10_68.dat',',',8,1);
Scan10_69 = dlmread('Scan10_69.dat',',',8,1);
Scan10_70 = dlmread('Scan10_70.dat',',',8,1);
Scan10_71 = dlmread('Scan10_71.dat',',',8,1);
Scan10_72 = dlmread('Scan10_72.dat',',',8,1);
Scan10_73 = dlmread('Scan10_73.dat',',',8,1);
Scan10_74 = dlmread('Scan10_74.dat',',',8,1);
Scan10_75 = dlmread('Scan10_75.dat',',',8,1);
Scan10_76 = dlmread('Scan10_76.dat',',',8,1);
Scan10_77 = dlmread('Scan10_77.dat',',',8,1);
Scan10_78 = dlmread('Scan10_78.dat',',',8,1);
Scan10_79 = dlmread('Scan10_79.dat',',',8,1);
Scan10_80 = dlmread('Scan10_80.dat',',',8,1);
```

```
Scan10_81 = dlmread('Scan10_81.dat',',',8,1);
Scan10_82 = dlmread('Scan10_82.dat',',',8,1);
Scan10_83 = dlmread('Scan10_83.dat',',',8,1);
Scan10_84 = dlmread('Scan10_84.dat',',',8,1);
Scan10_85 = dlmread('Scan10_85.dat',',',8,1);
Scan10_86 = dlmread('Scan10_86.dat',',',8,1);
Scan10_87 = dlmread('Scan10_87.dat',',',8,1);
Scan10_88 = dlmread('Scan10_88.dat',',',8,1);
Scan10_89 = dlmread('Scan10_89.dat',',',8,1);
Scan10_90 = dlmread('Scan10_90.dat',',',8,1);
Scan10_91 = dlmread('Scan10_91.dat',',',8,1);
Scan10_92 = dlmread('Scan10_92.dat',',',8,1);
Scan10_93 = dlmread('Scan10_93.dat',',',8,1);
Scan10_94 = dlmread('Scan10_94.dat',',',8,1);
Scan10_95 = dlmread('Scan10_95.dat',',',8,1);
Scan10_96 = dlmread('Scan10_96.dat',',',8,1);
Scan10_97 = dlmread('Scan10_97.dat',',',8,1);
Scan10_98 = dlmread('Scan10_98.dat',',',8,1);
Scan10_99 = dlmread('Scan10_99.dat',',',8,1);
Scan10_100 = dlmread('Scan10_100.dat',',',8,1);

Scan10 = [Scan10_1 Scan10_2    Scan10_3    Scan10_4
Scan10_5    Scan10_6    Scan10_7    Scan10_8    Scan10_9
Scan10_10   Scan10_11   Scan10_12   Scan10_13   Scan10_14
Scan10_15   Scan10_16   Scan10_17   Scan10_18   Scan10_19
Scan10_20   Scan10_21   Scan10_22   Scan10_23   Scan10_24
Scan10_25   Scan10_26   Scan10_27   Scan10_28   Scan10_29
Scan10_30   Scan10_31   Scan10_32   Scan10_33   Scan10_34
Scan10_35   Scan10_36   Scan10_37   Scan10_38   Scan10_39
Scan10_40   Scan10_41   Scan10_42   Scan10_43   Scan10_44
Scan10_45   Scan10_46   Scan10_47   Scan10_48   Scan10_49
Scan10_50   Scan10_51   Scan10_52   Scan10_53   Scan10_54
Scan10_55   Scan10_56   Scan10_57   Scan10_58   Scan10_59
Scan10_60   Scan10_61   Scan10_62   Scan10_63   Scan10_64
Scan10_65   Scan10_66   Scan10_67   Scan10_68   Scan10_69
Scan10_70   Scan10_71   Scan10_72   Scan10_73   Scan10_74
Scan10_75   Scan10_76   Scan10_77   Scan10_78   Scan10_79
Scan10_80   Scan10_81   Scan10_82   Scan10_83   Scan10_84
Scan10_85   Scan10_86   Scan10_87   Scan10_88   Scan10_89
Scan10_90   Scan10_91   Scan10_92   Scan10_93   Scan10_94
Scan10_95   Scan10_96   Scan10_97   Scan10_98   Scan10_99
Scan10_100];
```

```matlab
savefile = 'C:\Scan10\Scan10.mat';
save(savefile,'Scan10');
savefile = 'C:\Scan10\Scan10_time.mat';
save(savefile,'Scan10_time');

[C D] = size(Scan10);
for Cal_row = 1:C;
   for k_col = 1:D,
     Scan10_Cal(Cal_row,k_col) = CAL(Cal_row,1);
   end
end

%%%%%%%%%%%%Subtracting calibration%%%%%%%%%%%%%%%%%%%%%
Scan10_Obj = Scan10 - Scan10_Cal;
for Cal_row = 1:C;
   for k_col = 1:D,
     if (Scan10_Obj(Cal_row,k_col)<0),
        Scan10_Obj(Cal_row,k_col) = 0;
   else
        Scan10_Obj(Cal_row,k_col);
     end
   end
end

figure(1)
subplot(211);plot(Scan10_time,Scan10);xlabel('Number of
Points');ylabel('Magnitude');
subplot(212);plot(Scan10_time,Scan10_Obj);xlabel('Number of
Points');ylabel('Magnitude');
print -f -dtiff fig1

%%%%%%%%%%%%%%%Reflected peak selection%%%%%%%%%%%%%%%%%%
pick1 = 1:C;
for s = 1:D,
     Block_1 = Scan10_Obj(pick1,s);
    [a b] = max(Block_1);
    Max_scan(s,:) = a;
    Point_scan(s,:) = b;
end
```

```
%%%%%%%%%%%%%%Distance calculation%%%%%%%%%%%%%%%%%%%%%%%%
Speed_of_light = 21979245800;
for path = 1:D,
    Path_time(path,:) = Scan10_time(Point_scan(path,1),1);
end
  Distance_Scan10 = Speed_of_light.*(Path_time/2);

figure(2)
plot(Distance_Scan10,'x')
xlabel('Spatial step (cm)')
ylabel('Distance(cm)')
print -f -dtiff fig2

figure(3)
mesh(Scan10_Obj','x')
xlabel('Spatial step (cm)')
ylabel('Time(ns)')
zlabel('Magnitude')
print -f -dtiff fig3
```

APPENDIX B

MATLAB CODE (MC-II)

(FOR OBJECT RECONSTRUCTION UTILIZING MEASURED DATA)

```
clc;
clear all;
CAL = dlmread('Scan10_1.dat',',',8,1);
T = dlmread('Scan10_1.dat',',',8,0);
Scan10_time = T(:,1);
Scan10_1 = dlmread('Scan10_1.dat',',',8,1);
Scan10_2 = dlmread('Scan10_2.dat',',',8,1);
Scan10_3 = dlmread('Scan10_3.dat',',',8,1);
Scan10_4 = dlmread('Scan10_4.dat',',',8,1);
Scan10_5 = dlmread('Scan10_5.dat',',',8,1);
Scan10_6 = dlmread('Scan10_6.dat',',',8,1);
Scan10_7 = dlmread('Scan10_7.dat',',',8,1);
Scan10_8 = dlmread('Scan10_8.dat',',',8,1);
Scan10_9 = dlmread('Scan10_9.dat',',',8,1);
Scan10_10 = dlmread('Scan10_10.dat',',',8,1);
Scan10_11 = dlmread('Scan10_11.dat',',',8,1);
Scan10_12 = dlmread('Scan10_12.dat',',',8,1);
Scan10_13 = dlmread('Scan10_13.dat',',',8,1);
Scan10_14 = dlmread('Scan10_14.dat',',',8,1);
Scan10_15 = dlmread('Scan10_15.dat',',',8,1);
Scan10_16 = dlmread('Scan10_16.dat',',',8,1);
Scan10_17 = dlmread('Scan10_17.dat',',',8,1);
Scan10_18 = dlmread('Scan10_18.dat',',',8,1);
Scan10_19 = dlmread('Scan10_19.dat',',',8,1);
Scan10_20 = dlmread('Scan10_20.dat',',',8,1);

Scan10_21 = dlmread('Scan10_21.dat',',',8,1);
Scan10_22 = dlmread('Scan10_22.dat',',',8,1);
Scan10_23 = dlmread('Scan10_23.dat',',',8,1);
Scan10_24 = dlmread('Scan10_24.dat',',',8,1);
Scan10_25 = dlmread('Scan10_25.dat',',',8,1);
Scan10_26 = dlmread('Scan10_26.dat',',',8,1);
Scan10_27 = dlmread('Scan10_27.dat',',',8,1);
Scan10_28 = dlmread('Scan10_28.dat',',',8,1);
Scan10_29 = dlmread('Scan10_29.dat',',',8,1);
Scan10_30 = dlmread('Scan10_30.dat',',',8,1);
Scan10_31 = dlmread('Scan10_31.dat',',',8,1);
Scan10_32 = dlmread('Scan10_32.dat',',',8,1);
Scan10_33 = dlmread('Scan10_33.dat',',',8,1);
Scan10_34 = dlmread('Scan10_34.dat',',',8,1);
Scan10_35 = dlmread('Scan10_35.dat',',',8,1);
```

```
Scan10_36 = dlmread('Scan10_36.dat',',',8,1);
Scan10_37 = dlmread('Scan10_37.dat',',',8,1);
Scan10_38 = dlmread('Scan10_38.dat',',',8,1);
Scan10_39 = dlmread('Scan10_39.dat',',',8,1);
Scan10_40 = dlmread('Scan10_40.dat',',',8,1);

Scan10_41 = dlmread('Scan10_41.dat',',',8,1);
Scan10_42 = dlmread('Scan10_42.dat',',',8,1);
Scan10_43 = dlmread('Scan10_43.dat',',',8,1);
Scan10_44 = dlmread('Scan10_44.dat',',',8,1);
Scan10_45 = dlmread('Scan10_45.dat',',',8,1);
Scan10_46 = dlmread('Scan10_46.dat',',',8,1);
Scan10_47 = dlmread('Scan10_47.dat',',',8,1);
Scan10_48 = dlmread('Scan10_48.dat',',',8,1);
Scan10_49 = dlmread('Scan10_49.dat',',',8,1);
Scan10_50 = dlmread('Scan10_50.dat',',',8,1);
Scan10_51 = dlmread('Scan10_51.dat',',',8,1);
Scan10_52 = dlmread('Scan10_52.dat',',',8,1);
Scan10_53 = dlmread('Scan10_53.dat',',',8,1);
Scan10_54 = dlmread('Scan10_54.dat',',',8,1);
Scan10_55 = dlmread('Scan10_55.dat',',',8,1);
Scan10_56 = dlmread('Scan10_56.dat',',',8,1);
Scan10_57 = dlmread('Scan10_57.dat',',',8,1);
Scan10_58 = dlmread('Scan10_58.dat',',',8,1);
Scan10_59 = dlmread('Scan10_59.dat',',',8,1);
Scan10_60 = dlmread('Scan10_60.dat',',',8,1);

Scan10_61 = dlmread('Scan10_61.dat',',',8,1);
Scan10_62 = dlmread('Scan10_62.dat',',',8,1);
Scan10_63 = dlmread('Scan10_63.dat',',',8,1);
Scan10_64 = dlmread('Scan10_64.dat',',',8,1);
Scan10_65 = dlmread('Scan10_65.dat',',',8,1);
Scan10_66 = dlmread('Scan10_66.dat',',',8,1);
Scan10_67 = dlmread('Scan10_67.dat',',',8,1);
Scan10_68 = dlmread('Scan10_68.dat',',',8,1);
Scan10_69 = dlmread('Scan10_69.dat',',',8,1);
Scan10_70 = dlmread('Scan10_70.dat',',',8,1);
Scan10_71 = dlmread('Scan10_71.dat',',',8,1);
Scan10_72 = dlmread('Scan10_72.dat',',',8,1);
Scan10_73 = dlmread('Scan10_73.dat',',',8,1);
Scan10_74 = dlmread('Scan10_74.dat',',',8,1);
Scan10_75 = dlmread('Scan10_75.dat',',',8,1);
Scan10_76 = dlmread('Scan10_76.dat',',',8,1);
Scan10_77 = dlmread('Scan10_77.dat',',',8,1);
Scan10_78 = dlmread('Scan10_78.dat',',',8,1);
Scan10_79 = dlmread('Scan10_79.dat',',',8,1);
Scan10_80 = dlmread('Scan10_80.dat',',',8,1);
```

```
Scan10_81 = dlmread('Scan10_81.dat',',',8,1);
Scan10_82 = dlmread('Scan10_82.dat',',',8,1);
Scan10_83 = dlmread('Scan10_83.dat',',',8,1);
Scan10_84 = dlmread('Scan10_84.dat',',',8,1);
Scan10_85 = dlmread('Scan10_85.dat',',',8,1);
Scan10_86 = dlmread('Scan10_86.dat',',',8,1);
Scan10_87 = dlmread('Scan10_87.dat',',',8,1);
Scan10_88 = dlmread('Scan10_88.dat',',',8,1);
Scan10_89 = dlmread('Scan10_89.dat',',',8,1);
Scan10_90 = dlmread('Scan10_90.dat',',',8,1);
Scan10_91 = dlmread('Scan10_91.dat',',',8,1);
Scan10_92 = dlmread('Scan10_92.dat',',',8,1);
Scan10_93 = dlmread('Scan10_93.dat',',',8,1);
Scan10_94 = dlmread('Scan10_94.dat',',',8,1);
Scan10_95 = dlmread('Scan10_95.dat',',',8,1);
Scan10_96 = dlmread('Scan10_96.dat',',',8,1);
Scan10_97 = dlmread('Scan10_97.dat',',',8,1);
Scan10_98 = dlmread('Scan10_98.dat',',',8,1);
Scan10_99 = dlmread('Scan10_99.dat',',',8,1);
Scan10_100 = dlmread('Scan10_100.dat',',',8,1);

Scan10 = [Scan10_1 Scan10_2    Scan10_3    Scan10_4
Scan10_5    Scan10_6    Scan10_7    Scan10_8    Scan10_9
Scan10_10   Scan10_11   Scan10_12   Scan10_13   Scan10_14
Scan10_15   Scan10_16   Scan10_17   Scan10_18   Scan10_19
Scan10_20   Scan10_21   Scan10_22   Scan10_23   Scan10_24
Scan10_25   Scan10_26   Scan10_27   Scan10_28   Scan10_29
Scan10_30   Scan10_31   Scan10_32   Scan10_33   Scan10_34
Scan10_35   Scan10_36   Scan10_37   Scan10_38   Scan10_39
Scan10_40   Scan10_41   Scan10_42   Scan10_43   Scan10_44
Scan10_45   Scan10_46   Scan10_47   Scan10_48   Scan10_49
Scan10_50   Scan10_51   Scan10_52   Scan10_53   Scan10_54
Scan10_55   Scan10_56   Scan10_57   Scan10_58   Scan10_59
Scan10_60   Scan10_61   Scan10_62   Scan10_63   Scan10_64
Scan10_65   Scan10_66   Scan10_67   Scan10_68   Scan10_69
Scan10_70   Scan10_71   Scan10_72   Scan10_73   Scan10_74
Scan10_75   Scan10_76   Scan10_77   Scan10_78   Scan10_79
Scan10_80   Scan10_81   Scan10_82   Scan10_83   Scan10_84
Scan10_85   Scan10_86   Scan10_87   Scan10_88   Scan10_89
Scan10_90   Scan10_91   Scan10_92   Scan10_93   Scan10_94
Scan10_95   Scan10_96   Scan10_97   Scan10_98   Scan10_99
Scan10_100];
```

```matlab
savefile = 'C:\Scan10\Scan10.mat';
save(savefile,'Scan10');
savefile = 'C:\Scan10\Scan10_time.mat';
save(savefile,'Scan10_time');

load ('Cyl_Scan10_Total.mat');
load ('Cyl_Scan10_time.mat');
Cyl_Scan10_Total = Cyl_Scan10_Total(:,1:14250);
[C D] = size(Cyl_Scan10_Total);

pick1 = 1:C;
for s = 1:D,
    Block_1 = Cyl_Scan10_Total(pick1,s);
    [a b] = max(Block_1);
    Max_scan(s,:) = a;
    Point_scan(s,:) = b;
    Cyl_Scan10_Total(pick1,s) = Block_1;
End

%%%%%%%%%%%%%Distance calculation%%%%%%%%%%%%%%%%%%%%%%%%%%%%
Speed_of_light = 21979245800;
for path = 1:D,
 Path_time(path,:) = Cyl_Scan10_time(Point_scan(path,1),1);
end
 Distance_Cyl_Scan10_Total = Speed_of_light.*(Path_time/2);

%%%%%%%%%%%%%%%Maximum Thresholding%%%%%%%%%%%%%%%%%%%%%%%%%%
 for m1 = 1:D-4,
 if (Max_scan(m1+2,1)>= Max_scan(m1,1)&& Max_scan(m1+2,1)>=
Max_scan(m1+1,1))&&Max_scan(m1+2,1)>=
Max_scan(m1+3,1)&&Max_scan(m1+2,1)>=
Max_scan(m1+4,1)&&Max_scan(m1+2,1)>0.91,
     n1(m1+2,1) = m1+2;
 end
 end
 [M1 N1] = find(n1~=0);
 [M2 N2] = size(M1);
 for i_M1 = 1:M2-1,
       M3(i_M1,1) = M1(i_M1+1,1) - M1(i_M1,1);
 end
 M4 = find(M3>5);
 [M41 N41] = size(M4);
 for i_M4 = 1:M41,
    M5(i_M4,1) = M1(M4(i_M4,1),1);
end
```

```
[M51 N51] = size(M5);
  st3 = rem(M51,2);
    if (st3 == 0)
        M51 = M51;
    else
        M51 = M51-1;
    end
  M5 = M5(1:M51,1);
 Distance_peak = Distance_Cyl_Scan10_Total(M5,1);
 Cyl_Scan10_Total5 = Cyl_Scan10_Total(:,M5);
 for i_M5 = 1:M51-1,
    M6(i_M5,1) = floor((M5(i_M5+1,1)+M5(i_M5,1))/2);
 end
 M6 = [1;M6];
[M61 N61] = size(M6);
i_M6 = 1;
for i_M6 = 1:M61-1,
    Block_M6 = Max_scan(M6(i_M6,1):M6(i_M6,1),1);
    Block_M61(i_M6,1) = Block_M6;
    i_M6 = i_M6+1;
end
savefile = 'C:\Cyl_Scan10\Cyl_Scan10_Total5.mat';
save(savefile,'Cyl_Scan10_Total5');

%%%%%%%%%%Object Reference%%%%%%%%%%%%%%%%%%%%%
[F1 E1] = size(Distance_peak);
Diameter_of_object = 1.27;
Cal_Center_distance =
min(Distance_peak)+(max(Distance_peak)-
min(Distance_peak)+Diameter_of_object)/2;
Ref_Center_distance = Cal_Center_distance;

 %%%%%%%Initialized Rotation%%%%%%%%
Circular = min(Distance_peak);
[m2,n] = find(Distance_peak == Circular);
[m21 m22] = size(m2);
Initial_point = floor((m2(1,1)+m2(end,1))/2);
Block_3 = Distance_peak(Initial_point:F1,1);
Initial_Distance = [Block_3;
Distance_peak(1:Initial_point-1,1)];

%%%%%%%Find the longest diameter of the object%%%%%%%%%%%
[G H] = size(Initial_Distance);
for i = 1:G/2,
     D_Obj(i,1) = abs((2.*Ref_Center_distance)-
((Initial_Distance(i,1))+(Initial_Distance(i+G/2,1))));
end
```

```
[Ref_circle_diameter Point] = min(D_Obj);
[D_length D1] = size(D_Obj);
 Ref_Circle_distance = Initial_Distance(Point,1);
 Theta = Point*2*pi/G; Theta5 = Point*2*pi/G*180/pi
 L = abs(Ref_Center_distance-Ref_Circle_distance);
 R2 = Ref_circle_diameter/2;
      if Ref_Circle_distance < Ref_Center_distance,
         R_Center_Ref_Circle = abs((abs(L-R2))/(sin((pi/2)-
Theta)));
      else  if Ref_Circle_distance > Ref_Center_distance,
         R_Center_Ref_Circle = abs((L+R2)/(sin(Theta)-
(pi/2)));
             end
      end

%%%%%%%%%%%%%%% Object radius calculation %%%%%%%%%%%%%%%%
Ref_Circle_lengtth1(i,1)=0;
    for i = 0:(G-1),
Theta_1(i+1,1)= i*2*pi/G;
Theta_2(i+1,1) = (pi-Theta_1(i+1,1))/2;
Ref_Circle_lengtth1(i+1,1) =
((R_Center_Ref_Circle*sin((pi/2)-(Theta_1(i+1,1))))));
Ref_Circle_Distance_1(i+1,1) = Ref_Center_distance -
Ref_Circle_lengtth1(i+1,1);
    end
rho = (Ref_Circle_Distance_1 - (Initial_Distance));
[S_11 S_2] = find(Initial_Distance == Distance_peak(1,1));
S_1 = S_11(1,1);
Y11 = [Ref_Circle_Distance_1((S_1(1,1)+1):end,1);
zeros(S_1(1,1),1)];
Y22 = [zeros(G-S_1(1,1),1);
Ref_Circle_Distance_1(1:S_1(1,1))];
Ref_Circle_Distance_31 = Y11 + Y22;
rho = (Ref_Circle_Distance_1 - Initial_Distance);
rho1 = (Ref_Circle_Distance_31 - Distance_peak);
Avg_obj_radius = mean(rho)
rho2 = 0.635*ones(G,1);
    for i = 1:G-1;
        Theta_3(i+1,1)= i*2*pi/G;
    end
G1 = 1:G;
```

```
figure(1)
plot(G1,Ref_Circle_Distance_31,'-r')
hold on
plot(G1,Distance_peak,'-b')
hold off

figure(2)
plot(G1,Ref_Circle_Distance_1,'-r')
hold on
plot(G1,Initial_Distance,'-b')
hold off

figure(3)
polar(Theta_3,rho,'k-')
hold on
polar(Theta_3,rho2,'r-')
hold off

figure(4)
mmpolar(Theta_3,rho,'b--',Theta_3,rho2,'r-','grid','on')
mmpolar('border','on','rlimit',[-1 3])
mmpolar('RTickValue',[-1 0 1 2 3],'TTickValue',[0 30 60 90
120 150 180 210 240 270 300 330],'ttickdelta',30)
mmpolar(Theta_3,rho,'.k',Theta_3,rho2,'.r')
hold on

figure(5)
polar(Theta_3,rho1,'.r')
hold off
```

BIBLIOGRAPHY

[1]. E. C. Fear, Jeff Sill, Maria A. Stuchly, *Experimental Feasibility Study of Confocal Microwave Imaging for Breast Tumor Detection*, IEEE Trans. Microwave Theory Tech., vol.51, pp. 887-892, Mar. 2003.

[2]. E. C. Fear, Xu Li, S. C. Hagness, and M. A. Stuchly, *Confocal Microwave Imaging for Breast Cancer Detection: Localization of Tumors in Three Dimensions*, IEEE Trans. Biomed. Eng., vol. 49, pp. 812-822, 2002.

[3]. E. C. Fear, Susan C. Hagness, Paul M. Meaney, Michal Okoniewski, Maria A. Stuchly, *Enhancing Breast Tumor Detection with Near-Field Imaging*, IEEE microwave magazine, pp. 48-56, 2002.

[4]. X. Chen and K. Huang, *Microwave Imaging of Buried Inhomogeneous Objects Using Parallel Genetic Algorithm Combined with FDTD Method*, Progress in Electromagnetics Research, PIER 53, 283-298, 2005

[5]. W. C. Khor, H. Wang, M. E. Bialkowski and S. Crozier, *Experimental and theoretical investigations into a microwave breast cancer detection system*, 17th International Zurich Symposium on Electromagnetic Compatibility, pp. 105-108, 2006

[6]. Isaac N. Bankman, William A. Christens-Barry, Irvign N. Weinberg, Dong W. Kim, Ralph D. Semmel, and William R. Brody, *An Algorithm for Early Breast Cancer Detection in Mammograms*, Fifth Annual IEEE Symposium on Computer-Based Medical Systems, Session 6A-B; Frontiers Detection of Cancer, 1992.

[7]. Tania Stathaki, and A.G. Constantinides, *Neural Networks and Higher Order Spectra for Breast Cancer Detection*, IEEE, 1994.

[8]. Parvis Gamagami, Melvin J. Silverstein, and James R. Waisman, *Infra-red imaging in Breast Cancer*, 19th International Conference, IEEE/EMBS, 1997.

[9]. E.C. Fear, and M.A. Stuchly, *Microwave Breast Cancer Detection*, 2000 IEEE MTT-S Digest, 2000.

[10]. Tobias Christian Cahoon, Melanie A. Sutton, and James C. Bezdek, *Breast Cancer Detection using Imaging Processing Techniques*, IEEE, 2000.

[11]. J.R. Keyserlingk, P.D. Ahlgren, E. Yu, N. Belliveau, M. Yassa, *Funtional Infrared Imaging of the Breast*, IEEE Engineering in Medicine and Biology, 2000.

[12]. Xu Li, and Susan C. Hagness, *A Confocal Microwave Imaging Algorithm for Breast Cancer Detection*, IEEE Microwave and Wireless components Letters, Vol.11, NO.3, 2001.

[13]. F.A. Cardillo, A. Starita, D. Caramella, A. Cilotti, *A Neural Tool for Breast Cancer Dtection and Classification in MRI*, 2001 Proceedings of the 23rd Annual EMBS International Conferecne, Turkey, 2001.

[14]. Ziji Wu and John M. Sullivan, Jr., *Automatic Finite Element Mesh Generation from MRI Scans for Breast Cancer Investigations*, Proceedings of the IEEE 27th Annual Northeast Bioengineering Conference, 2001.

[15]. Wael Saleh and Nasser Qaddoumi, *Breast Cancer Detection Using Non-invasive Near-field Microwave Nondestructive Testing Techniques*, ICES-2003 IEEE, 2003.

[16]. R.S. Yoon, T.P. Demonte, L. Organ, M.L.G. Joy, *Study of Current Density Distribution in a Non-invasive Breast Cancer Detection Device*, Proceedings of the 25th Annual International Conference of the IEEE EMBS, 2003.

[17]. Xing Yun, Elise C. Fear and Ronald Johnston, *Broadband Cross-Polarized Bowtie Antenna for Breast Cancer Detection*, IEEE, 2003.

[18]. Panagiotis Kosmas, Carey M. Rappaport, and Emmett Bishop, *Modeling with the FDTD Method for Microwave Breast Cancer Detection*, IEEE Transactions on Microwave Theory and Techniqes, Vol.52, NO.8, August 2004.

[19]. Myong H. Dhoi, Tzu-Jen Kao, David Isaacson, Gary J. Saulnier, and Jonathan C. Newell, *A Simplified Model of Mammography Geometry for Breast Cancer Imaging with Electrical Impedance Tomography*, Proceeding of the 26th Annual International Conference of the IEEE EMBS, September 2004.

[20]. Jeff M. Sill, and Elise C. Fear, *Tissue Sensing Adaptive Radar for Breast Cancer Detection-Experimental Investigation of Simple Tumor Models*, IEEE Transactions on Microwave Theory and Techniques, Vol.53, NO.11, November 2005.

[21]. Xu Li, Essex J. Bond, Barry D, Ban Veen, and Susan C. Hagness, *An Overview of Ultra-Wideband Microwave Imaging via Space-Time Beamforming for Early-Stage Breast-Cancer Detection*, IEEE Antennas and Propagation Magazine, Vol.47, No. 1, February 2005.

[22]. Wanjun Zhi, Francois Chin, and Michael Yan-Wah Chia, *Near Field Imaging for Breast Cancer Detection by UWB Minimum Variance Beamforming*, IEEE, 2006.

[23]. John D. Kraus, Ronald J. Marhefka, *Antennas for all Applications*, Tata McGraw-Hill, New Delhi, 2003.

[24]. Constantine A. Balanis, *Antenna Theory Analysis and Design*, John Wiley & Sons, Inc., New Jersey, 2005.

[25]. David M. Pozar, *Microwave and RF Design of Wireless Systems*, John Wiley & Sons, Inc., New Jersey, 2001.

[26]. Constantine A. Balanis, *Advanced Engineering Electromagnetics*, John Wiley & Sons, Inc., New Jersey, 1989.

[27]. John G. Proakis, Dimitris G. Manolakis, *Digital Signal ProcessingPrinciples, Algorithms, and Applications*, Prentice-Hall, Inc., New Jersey, 1996.

[28]. Operating Manual, *NSI Lite Series Near-field Antenna Measurement System*, NSI Inc., Vol.1, September 16, 1996, 1330 E. 223rd St. Suite 524, Carson California, 90745 USA, Tel(310) 518-4277.

INDEX

mammograms, 3, 4
Maxwell's equation, 17
microwave, 1, 2, 9, 12, 27, 35, 77

N

near-field, 1, 2, 8, 9, 10, 11, 25, 63
Normal Incidence, 15
NSI, 2, 10, 11, 25, 34, 63, 79

O

oblique angles, 19
oblique wave incidence, 19

P

parallel polarization, 19, 24
perpendicular polarization, 19, 22
planar scan, 28, 30, 50, 52
pyramidal horn antenna, 2, 25, 38, 43

R

reflection, 15, 16, 17, 18, 21, 22, 24
reflection coefficient, 21, 24
rotational angle index, 56, 60
rotational index, 58, 61
Rotational scan, 29, 33, 53

S

scattering-matrix, 13
Single-Probe Detection and Reconstruction, 1
S-parameter, 11, 13, 25, 27, 34, 44, 45
SPDR, 1, 30, 58, 60, 61, 63, 64
subtracting method, 48

T

transmission, 15, 16, 17, 18, 21, 22, 24

U

ultrawideband, 4

V

VSWR, 14

W

wave equation, 16
Wave impedance, 18
wave propagation, 15, 40
waveguide, 5, 12, 14, 25, 27, 35, 40, 46, 50, 53, 56